Biological Cybernetics
https://doi.org/10.1007/s00422-021-00893-7

Biological Cybernetics

ORIGINAL ARTICLE

A dynamic neural field model of continuous input integration

Weronika Wojtak[1,2] · **Stephen Coombes**[3] · **Daniele Avitabile**[4,5] · **Estela Bicho**[2] · **Wolfram Erlhagen**[1]

Received: 1 April 2021 / Accepted: 1 August 2021

Abstract
The ability of neural systems to turn transient inputs into persistent changes in activity is thought to be a fundamental requirement for higher cognitive functions. In continuous attractor networks frequently used to model working memory or decision making tasks, the persistent activity settles to a stable pattern with the stereotyped shape of a "bump" independent of integration time or input strength. Here, we investigate a new bump attractor model in which the bump width and amplitude not only reflect qualitative and quantitative characteristics of a preceding input but also the continuous integration of evidence over longer timescales. The model is formalized by two coupled dynamic field equations of Amari-type which combine recurrent interactions mediated by a Mexican-hat connectivity with local feedback mechanisms that balance excitation and inhibition. We analyze the existence, stability and bifurcation structure of single and multi-bump solutions and discuss the relevance of their input dependence to modeling cognitive functions. We then systematically compare the pattern formation process of the two-field model with the classical Amari model. The results reveal that the balanced local feedback mechanisms facilitate the encoding and maintenance of multi-item memories. The existence of stable subthreshold bumps suggests that different to the Amari model, the suppression effect of neighboring bumps in the range of lateral competition may not lead to a complete loss of information. Moreover, bumps with larger amplitude are less vulnerable to noise-induced drifts and distance-dependent interaction effects resulting in more faithful memory representations over time.

Keywords dynamic neural field · conservation law · localized states · stability · input integration

1 Introduction

The ability of the brain to accumulate, combine and maintain information over behaviorally relevant time scales is fundamental for a wide variety of cognitive functions that bridge perception and action (Miller and Cohen 2001). This has been associated with persistent neural activity observed in many brain regions in working memory, decision making or planning tasks (Curtis and Lee 2010). The longstanding hypothesis that reverberations in recurrent neural networks can give rise to sustained activity throughout periods without external stimulation (Hebb 1949) has motivated an impressive amount of experimental and computational modeling work (for reviews see Wang 2003; Zylberberg and Strowbridge 2017). A particularly insightful theoretical framework has been the continuous bump attractor network (Amari 1977; Brody et al. 2003b; Compte et al. 2000) which has been widely used in the past to explain data from

Communicated by Benjamin Lindner.

✉ Weronika Wojtak
w.wojtak@dei.uminho.pt

Stephen Coombes
stephen.coombes@nottingham.ac.uk

Daniele Avitabile
d.avitabile@vu.nl

Estela Bicho
estela.bicho@dei.uminho.pt

Wolfram Erlhagen
wolfram.erlhagen@math.uminho.pt

1 Research Centre of Mathematics, University of Minho, Guimarães, Portugal

2 Research Centre Algoritmi, University of Minho, Guimarães, Portugal

3 Centre for Mathematical Medicine and Biology, School of Mathematical Sciences, University of Nottingham, Nottingham, UK

4 Department of Mathematics, Vrije Universiteit, Amsterdam, The Netherlands

5 MathNeuro Team, Inria Sophia Antipolis Méditerranée Research Centre, Sophia Antipolis, France

Published online: 21 August 2021

behavioral experiments and to synthesize cognitive behavior in robotics systems (Erlhagen and Bicho 2006; Schöner 2016). It explains the emergence of stable representations of continuous-valued information, such as for example the direction of heading during navigation or the position of an object in space, by assuming a distance-dependent neuronal connectivity pattern in feature space. Typically, neurons tuned to similar values of a continuous variable excite each other, and those tuned to dissimilar values inhibit each other. When the neurons are ordered along a line by their selectivity, the self-stabilized activity pattern, which the intrinsic network dynamics develops in response to a transient input, is visualized as a spatially localized activity bump. Due to the assumed translation-invariant connection structure, the network can hold a continuous family of bumps, with each of the attractor states representing the memory of a specific input value. Continuous attractor networks provide some degree of robustness to perturbations away from the attractor manifold since perturbed network activity quickly decays back to the bump state. However, since bumps are neutrally stable, their position can be easily shifted along the manifold by weak external inputs (Amari 1977). This property can be exploited for instance to explain the capacity of a neural system to track the position of a moving object in real time (Wu et al. 2008), and for a robotics application (see also Bicho et al. 2000). Direct experimental evidence for a continuous bump attractor hypothesis comes from visuo-spatial working memory (WM) tasks in which a subject has to maintain the information about the spatial position of one or more objects over a short period of time. After the cessation of the tuned external input, the bump position is vulnerable to random activity fluctuations which may cause a drift of the bump over time (Camperi and Wang 1998; Kilpatrick and Ermentrout 2013). This model-derived predictive relationship between persistent neural population activity and the variability of spatial memory over time has been reported recently in a combined electrophysiological and behavioral task (Wimmer et al. 2014). Consistent with the neural dynamics in continuous attractor models of multi-item memory (Amari 1980; Ferreira et al. 2016; Krishnan et al. 2018), several behavioral experiments report distance-dependent interaction effects between memory traces which may be described as an attractive or repulsive bias of memorized nearby items (Almeida et al. 2015; Johnson et al. 2009, for a discussion of the neural underpinning of attraction versus repulsion see also Erlhagen et al. 1999).

Despite their success in many applications, the explanatory power of classical continuous attractor models remains still limited since the memory bump has a stereotyped shape exclusively determined by the recurrent interactions within the network. A more sophisticated circuit-based model should regulate also the shape and rate of localized persistent activity depending on the qualitative and quantitative characteristics of the preceding inputs. It has been shown for instance that the level of persistent activity during the delay period of a spatial WM task correlates with stimulus contrast (Constantinidis et al. 2001) and can be modulated by additional spatially informative cues (Kuo et al. 2012; Wildegger et al. 2016). Importantly, the discharge rate of neural populations is predictive of the psychophysical task performance. The notion of a static bump as a neural correlate of WM is also inconsistent with recent evidence showing that persistent input-selective activity often changes systematically during the course of the delay period (e.g., ramping-type activity (Brody et al. 2003b)). One hypothesis is that the variability in activity is due to the continuous integration of other task relevant information such as for instance the time elapsed since stimulus presentation (Brody et al. 2003a). The capacity of neural circuits to rapidly change firing rates in response to transient inputs while maintaining firing at a constant level for extended periods of time is fundamental for decision making processes (Curtis and Lee 2010; Sakai et al. 2006). This requires the accumulation and storage of evidence for competing options across time. Neural recordings from animals suggest that the level of activity of neural populations representing a certain option correlates with choice certainty (Kiani and Shadlen 2009). The observation that persistent activity related to the outcome of previous choices often continues during inter-trial intervals shows that the integration time can be quite long (Histed et al. 2009).

Here, we analyze a new bump attractor model (Wojtak et al. 2016) based on the theoretical framework of dynamic neural fields that is able to hold in addition to a continuum of bump positions also a continuum of bump amplitudes. The construction of recurrent networks that can transform brief inputs into sustained firing rates at different levels has been proven to be a nontrivial problem (Koulakov et al. 2002; Sakai et al. 2006). Previous work was based on the assumption of networks with linear input-output functions or, when more realistic nonlinear neurons were used, heavily relied on numerical fine tuning of network parameters (Brody et al. 2003b; Seung 1998). A balanced relation of excitation and inhibition in the network must be kept so that the sustained activity at any time represents the time integral of past inputs. A recent dynamic field model addresses the existence of bumps with varying amplitudes in a lateral inhibition network with separate excitatory and inhibitory populations and a piecewise linear firing rate function (Carroll et al. 2014). To support a range of possible bump amplitudes, the recurrent excitation must be precisely chosen to be inversely proportional to the gain of the transfer function. To mitigate this fine tuning problem, additional mechanisms such as the use of bistable neurons with different activation thresholds have been proposed (Koulakov et al. 2002), for review of different computational approaches see (Sakai et al. 2006). Due to the bistability, the integrator network exhibits multi-

ple stable states even with imprecisely tuned feedback. The inherent trade-off is a loss of sensitivity to weaker input since a minimum input strength is necessary to transition between adjacent states.

Our proposed model does not rely on a domain of linear input-output transfer and supports in principle a continuous integration of inputs of any strength and duration. It consists of two coupled dynamic fields of Amari type (Amari 1977). The field receiving external input has a classical Mexican-hat coupling with excitation dominating at short distances and surround inhibition. The second field integrates the activity from the first field with an inverted Mexican-hat connectivity and feeds its activity back locally. We first analyze the existence, stability and bifurcation structure of bumps with input-dependent shapes and discuss their relevance to modeling cognitive functions such as working memory and decision making. We then systematically compare the pattern formation process in the Amari and the two-field model in tasks with multiple localized inputs. Specifically, we are interested in evaluating how the local feedback mechanisms of the two-field model affect the interaction of nearby bumps and the robustness of memory maintenance in the presence of random activity fluctuations.

2 Definition of the two-field model

We study a system of two coupled neural field equations defined on a one-dimensional finite domain $\Omega : [-L, L]$:

$$\begin{aligned}\frac{\partial u(x,t)}{\partial t} &= -u(x,t) + v(x,t) + I(x,t) \\ &\quad + \int_\Omega w(|x-y|) f(u(y,t)-\theta)\mathrm{d}y, \end{aligned} \tag{1a}$$

$$\begin{aligned}\tau_v \frac{\partial v(x,t)}{\partial t} &= -v(x,t) + u(x,t) \\ &\quad - \int_\Omega w(|x-y|) f(u(y,t)-\theta)\mathrm{d}y. \end{aligned} \tag{1b}$$

Here the variables $u(x,t)$ and $v(x,t)$ represent the activity (e.g., membrane potential) of a neuron at the spatial location x at time t in two coupled populations, labeled u and v, respectively. The firing rate function $f(x)$ is chosen as a Heaviside function with threshold θ such that $f(x) = 1$ for $x \geq 0$ and $f(x) = 0$ otherwise. The weight function $w(|x-y|)$ representing the synaptic connectivity between neurons at locations x and y has a Mexican-hat shape given by the difference of two Gaussian functions:

$$w(x) = A_{ex} e^{\left(-x^2/2\sigma_{ex}^2\right)} - A_{in} e^{\left(-x^2/2\sigma_{in}^2\right)} - w_{inh}, \tag{2}$$

with $A_{ex} > A_{in} > 0$ and $\sigma_{in} > \sigma_{ex} > 0$. The parameter $w_{inh} > 0$ guarantees that spatially uniform inhibition exists at larger distances, $|x| > x_c$.

The time-dependent external input $I(x,t)$ to the u-population is modeled as one or more Gaussians centered at positions x_{c_j}:

$$I(x,t) = (H_{t_0}(t) - H_{t_e}(t)) \sum_{j=1}^{n} A_{I_j} e^{\left(-(x-x_{c_j})^2/2\sigma_{I_j}^2\right)}, \tag{3}$$

where $H_{t_0}(t)$ represents the Heaviside step function with threshold $t_0 \geq 0$ controlling the start and the end of the input at times t_0 and t_e, respectively. In the following we use for the input duration the notation $d_I = t_e - t_0$. Input strength is controlled by $A_{I_j} > 0$.

The u-equation of system (1) without the term $v(x,t)$ represents the field model originally introduced and analyzed by Amari (1977). He considers two separate inhibitory and excitatory subpopulations and derives the single population model with Mexican-hat connectivity by assuming that the wider ranging inhibitory feedback in the network is infinitely fast. This ensures that the spread of self-sustained excitation remains localized in a region activated by external input. Findings in neurophysiological and modeling studies of the cortical microcircuit of spatial WM stress the important role of local inhibitory feedback for generating persistent activity (Constantinidis and Wang 2004). A distinct subclass of interneurons has been described which integrates inputs from nearby excitatory cells and exhibits sustained responses with similar tuning properties during delay periods. As part of a feedback loop, these neurons might implement a tight balance of excitatory and inhibitory inputs to a target cell. Biologically plausible circuit models of WM have also addressed how cortical disinhibition of interneurons (e.g., by interneurons targeting interneurons) with different spatial tuning affect WM maintenance (Murray et al. 2014). The mechanistic two-field model implements a balanced local inhibitory feedback and a disinhibition of lateral inhibitory feedback by assuming that the v-population integrates the activity of the u-population with an inverted Mexican-hat connectivity. Note that a spatial integration with a Mexican-hat profile could be applied as well when $-v(x,t)$ instead of $+v(x,t)$ is used in the u-equation. To understand the role of the v-population in the pattern formation process, it is instructive to follow Amari's strategy and also consider different time scales for the two populations. In the limiting case $\tau_v \to 0$, the v-population is at quasi-equilibrium with

$$v(x,t) = u(x,t) - \int_\Omega w(|x-y|) f(u(y,t)-\theta)\mathrm{d}y. \tag{4}$$

Substituting this expression into the u-equation of (1) yields

$$\frac{\partial u(x,t)}{\partial t} = I(x,t). \tag{5}$$

The u-population thus implements a robust temporal integration of external inputs if fast inhibitory feedback loops counterbalance any input-induced changes in the recurrent interactions (Denève and Machens 2016; Lim and Goldman 2013). For the integration to be perfect, we have to assume a linear response function of the v-population, $f(v) = v$. The presence of nonlinearities in the neural dynamics such as saturation will make the integrator circuit insensitive to additional input when the saturation limit of the response function $f(v)$ is reached (Lim and Goldman 2013). Notably, the integrator capacity does not depend on the precise choice of the connectivity function $w(x)$ or the nonlinearity $f(u)$. In the rest of the paper, we analyze and apply model (1) with identical timescales for the u-population and the v-population ($\tau_v = 1$). This allows us to directly compare the behavior of the two-field and the Amari models.

2.1 Existence and stability of one-bump solutions

2.1.1 Linear stability analysis à la Amari

In the following we study the existence and stability of single bump steady state solutions of the model (1) in the case of a Heaviside firing rate function and initial condition $u(x,0) + v(x,0) = K$, where $K > 0$ is a constant.
Let $R[u(x,t)]$ be the region over which the field is excited

$$R[u(x,t) > \theta] = (x_1(t), x_2(t)) \tag{6}$$

and let the gradients of $u(x,t)$ at the boundaries x_1 and x_2 of the excited region be

$$c_1 = \frac{\partial u(x_1,t)}{\partial x}, \qquad -c_2 = \frac{\partial u(x_2,t)}{\partial x}. \tag{7}$$

After a short period of time $\mathrm{d}t$ the excited region changes to

$$R[u(x,t+\mathrm{d}t)] = (x_1(t+\mathrm{d}t), x_2(t+\mathrm{d}t)). \tag{8}$$

The boundaries of the excited region satisfy

$$\text{at time } t: \quad u(x_i,t) = \theta, \tag{9a}$$
$$\text{at time } t+\mathrm{d}t: \quad u(x_i+\mathrm{d}x_i, t+\mathrm{d}t) = \theta, \tag{9b}$$

where $x_i(t+\mathrm{d}t) = x_i + \mathrm{d}x_i, i = 1,2$.
A Taylor expansion of the latter equation yields

$$\frac{\partial u(x_i,t)}{\partial x}\mathrm{d}x_i + \frac{\partial u(x_i,t)}{\partial t}\mathrm{d}t = 0, \qquad i = 1,2, \tag{10}$$

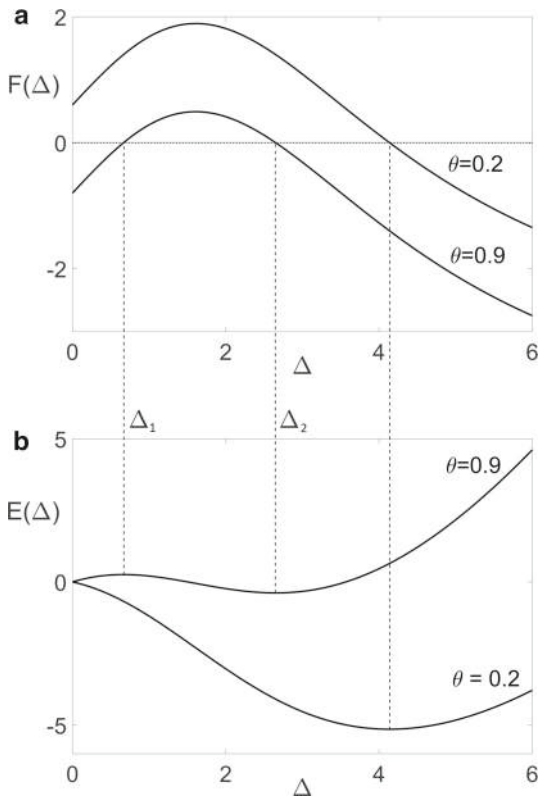

Fig. 1 **a** The plot of $F(\Delta)$ given by (16) with $K = 1$. For $\theta = 0.2$, there is one (stable) solution with $\Delta = 4.14$. For $\theta = 0.9$, there are two solutions: unstable solution with $\Delta = 0.67$ and stable solution with $\Delta = 2.65$. **b** The plot of $E(\Delta)$ given by (20). For $\theta = 0.2$, there is a local minimum with $\Delta = 4.14$. For $\theta = 0.9$, there is a local maximum with $\Delta = 0.67$ and a local minimum with $\Delta = 2.65$. The kernel w is given by (2) with $A_{ex} = 3$, $\sigma_{ex} = 1.4$, $A_{inh} = 1.5$, $\sigma_{inh} = 3$ and $w_{inh} = 0.2$

for infinitesimally small $\mathrm{d}x_i$ and $\mathrm{d}t$.
We can then rewrite (1) at $x = x_i(t)$ as

$$\frac{\partial u(x,t)}{\partial t} = -u(x,t) + v(x,t) + \int_{x_1(t)}^{x_2(t)} w(|x-y|)\mathrm{d}y, \tag{11a}$$
$$\frac{\partial v(x,t)}{\partial t} = -v(x,t) + u(x,t) - \int_{x_1(t)}^{x_2(t)} w(|x-y|)\mathrm{d}y. \tag{11b}$$

Let

$$W(x) = \int_0^x w(y)\mathrm{d}y. \tag{12}$$

Since $u(x_i,t) = \theta$, we have from (11a)

$$\frac{\partial u(x_i,t)}{\partial t} = -2\theta + K + W(x_2 - x_1). \tag{13}$$

We have

$$\frac{\mathrm{d}x_1}{\mathrm{d}t} = \left.\frac{-\partial u/\partial t}{\partial u/\partial x}\right|_{x=x_1} = -\frac{1}{c_1}\left(-2\theta + K + W(x_2 - x_1)\right), \tag{14a}$$

$$\frac{\mathrm{d}x_2}{\mathrm{d}t} = \left.\frac{\partial u/\partial t}{\partial u/\partial x}\right|_{x=x_2} = \frac{1}{c_2}\left(-2\theta + K + W(x_2 - x_1)\right). \tag{14b}$$

We can then describe the change of length of the excited region $\Delta(t) = x_2(t) - x_1(t)$

$$\frac{\mathrm{d}\Delta}{\mathrm{d}t} = \left(\frac{1}{c_1} + \frac{1}{c_2}\right)\left(-2\theta + K + W(\Delta)\right). \tag{15}$$

The existence of solution of width $\Delta = x_2 - x_1$ is determined by the roots of

$$F(\Delta) = -2\theta + K + W(\Delta) = 0. \tag{16}$$

The stability condition is that a steady state of width Δ is stable if

$$\frac{\mathrm{d}F(\Delta)}{\mathrm{d}\Delta} < 0, \tag{17}$$

and unstable otherwise. We plot examples of function $F(\Delta)$ for different values of threshold θ in Fig. 1a.

2.1.2 Lyapunov method

The stability of bump solutions can be also analyzed by searching for local minima and local maxima of a Lyapunov functional associated with system (1) (French 2004; Kubota and Aihara 2005; Owen et al. 2007). For the two-field model with Heaviside firing rate function, the functional is given by

$$\begin{aligned} E[u] = &-\frac{1}{2}\int_\Omega\int_\Omega w(|x-y|)\, f(u(x,t)-\theta) \\ &\times f(u(y,t)-\theta)\mathrm{d}x\mathrm{d}y \\ &+ (2\theta - K)\int_\Omega f(u(x,t)-\theta)\mathrm{d}x. \end{aligned} \tag{18}$$

For a bump of width $\Delta = (x_2 - x_1)$ we have

$$\begin{aligned} E(\Delta) = &-\frac{1}{2}\int_{x_1}^{x_2}\int_{x_1}^{x_2} w(|x-y|)\mathrm{d}x\mathrm{d}y \\ &+ (2\theta - K)\,(x_2 - x_1). \end{aligned} \tag{19}$$

Using (12) we obtain

$$E(\Delta) = -\int_0^\Delta W(x)\mathrm{d}x + (2\theta - K)\,\Delta. \tag{20}$$

Figure 1b shows plots of $E(\Delta)$ for the example used in Fig. 1a. As indicated by the vertical lines, the local minima correspond to stable and the local maxima to unstable bumps.

3 Steady states of the model in the absence of input

3.1 Bumps with initial condition $u(x, 0) + v(x, 0) = K$

We start the numerical investigation of one-bump solutions of the two-field model using the symmetric initial condition

$$u(x,0) = A_u e^{\left(-x^2/2\sigma_u^2\right)}, \quad v(x,0) = K - u(x,0), \tag{21}$$

where $A_u > 0$, $\sigma_u > 0$ and $K \geq 0$. Stable bumps are found by numerically integrating (1) to a steady state. Following the numerical analysis of the Amari model (Amari 1980), we expect convergence if the width of the initial profile above threshold exceeds the width Δ_1 of the unstable pattern in Fig. 1. To find the unstable bump associated with a narrower initial profile, we apply numerical bifurcation techniques described in (Rankin et al. 2014). These techniques also allow us to track steady states of (1) when model parameters are varied. The bifurcation curve in Fig. 2a with the threshold θ as continuation parameter shows that for $K < 2\theta$ branches of stable (solid line) and unstable (dashed line) bumps coexist. For $K \geq 2\theta$, the unique steady state is a stable bump. The panels on the right show particular solutions as indicated by the points P_1, P_2 and P_3 on the bifurcation curve. Here and in all following figures, solid and dashed black lines represent $u(x)$ and $v(x)$, respectively. Like for the Amari model, the shape of the bump attractor does not depend on the shape of the initial profile (compare panels (d) and (e)). Note that for a subthreshold initial profile, $A_u < \theta$, the activity converges to the homogeneous solution $(u, v) = (K/2, K/2)$.

3.2 Bumps with initial condition $u(x, 0) + v(x, 0) = K(x)$

To work as a neural integrator, the bump shape of the two-field model (1) should depend on the initial conditions for the u-population and the v-population since they may be set by external input. Figure 3 shows examples of bump solutions for the initial conditions

$$u(x,0) = K(x), \quad v(x,0) = 0, \quad K(x) = A_K e^{\left(-x^2/2\sigma_K^2\right)}, \tag{22}$$

which represent a homogeneous initial state for the v-population and a spatially structured state for the u-population.

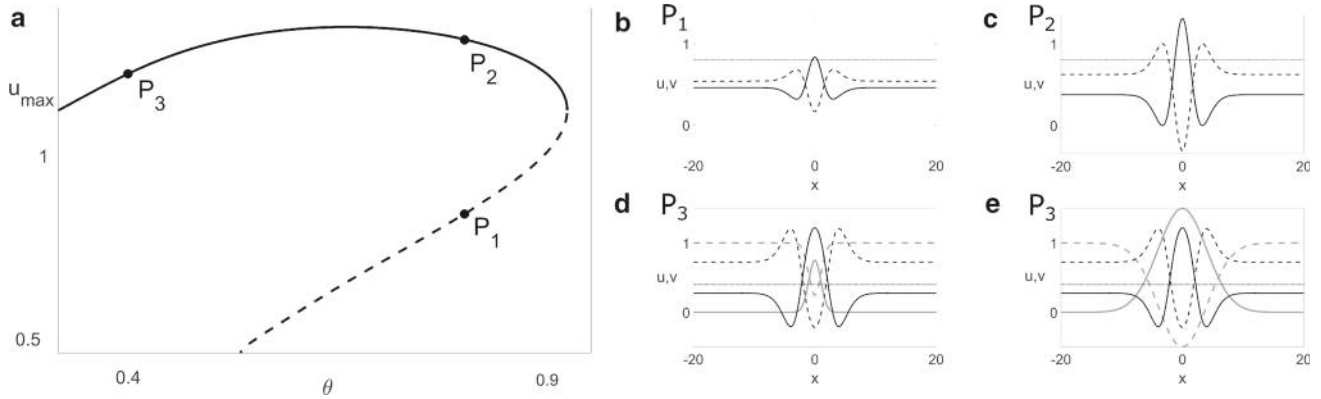

Fig. 2 **a** Bifurcation curve showing one-bump solutions of (1) with a Mexican-hat kernel (2) as the threshold parameter θ is varied. Solid (dashed) lines represent stable (unstable) solutions. u_{max} is the maximum of u over all x. (**b**-**e**) Examples of solutions at the points P_1 (unstable) and P_2 (stable) for $\theta = 0.8$ (dotted line) and P_3 (stable) for $\theta = 0.4$ (dotted line) are shown. Solid and dashed black lines represent $u(x)$ and $v(x)$, respectively. For the solution at the point P_3 we show examples of different initial conditions, with solid (dashed) grey lines representing initial profiles $u(x, 0)$ ($v(x, 0)$). They are given by (21) with $A_u = 0.75$, $\sigma_u = 1$, $K = 1$ (**d**) and $A_u = 1.5$, $\sigma_u = 4$, $K = 1$ (**e**). For the remaining solutions, the initial condition is given by (21) with $A_u = 1$ and $\sigma_u = 1$, $K = 1$. The kernel w is given by (2) with $A_{ex} = 2$, $A_{in} = 1$, $\sigma_{ex} = 1.25$, $\sigma_{in} = 2.5$ and $w_{inh} = 0.1$

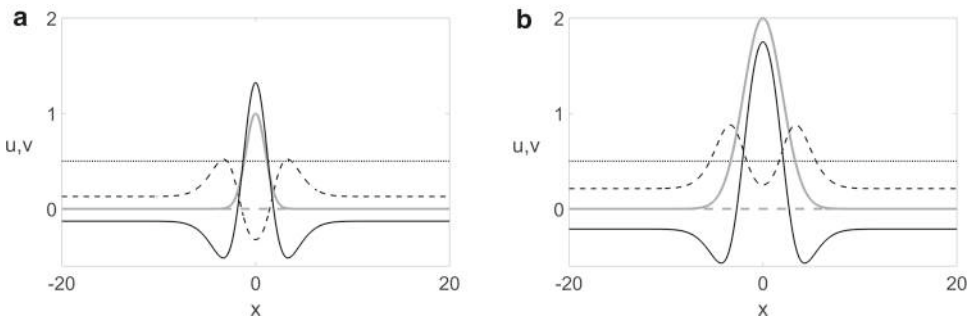

Fig. 3 One-bump solution of the two-field model (1) (black lines) for two different initial profiles (22) (grey lines) with $A_K = 1$, $\sigma_K = 1$ (**a**) and $A_K = 2$, $\sigma_K = 2$ (**b**). Parameters of the kernel as in Fig. 2. Threshold $\theta = 0.5$ (dotted line)

As can be clearly seen when comparing the activation patterns in the two panels, the bump shape correlates perfectly with the shape of the initial activation profile of the u-population.

Figure 4 shows results of numerical continuation of bump solutions of (1) with initial condition (22) and threshold θ as a continuation parameter.

The bifurcation curves for the smaller (a) and the larger (c) initial profiles are different but maintain the same qualitative features. Again we can see that in a certain range of threshold values stable and unstable bumps coexist. However, different to the case of the symmetric initial condition (21), there is an additional branch of stable subthreshold bumps given by $u(x, t) = v(x, t) = K(x)/2$. Panels (b) and (d) show examples of the three types of bump solutions at the points P_1, P_2 and P_3 of the bifurcation curves. It can be seen that a larger initial profile leads to larger bumps and shifts their coexistence to higher threshold values. In the example, the width and the amplitude of the initial profile were manipulated affecting both the width and the amplitude of the evolving pattern. It is important to notice that stable bumps with a constant width and varying amplitude can be created for instance with a truncated Gaussian profile which limits the spatial range of the initial activation. We come back to this point when discussing the continuous integration of localized inputs of varying duration and strength in Sect. 4.

3.3 Multi-bump solutions

3.3.1 Numerical continuation of two-bump solutions

Different from the Amari model (Laing and Troy 2003), the two-field model supports the existence of stable two-bump solutions for which the inter-peak distance is within the competitive range of the Mexican-hat connectivity. We use numerical continuation to track two-bump solutions of (1) as the threshold parameter θ varies. Figure 5 shows the resulting bifurcation curve with stable and unstable suprathreshold branches and a subthreshold branch. Different to the situation for single bumps, the subthreshold solution (P1) does not coexist with the suprathreshold two-bumps (P3 and P4). To evaluate the dependence of the inter-peak distance on model

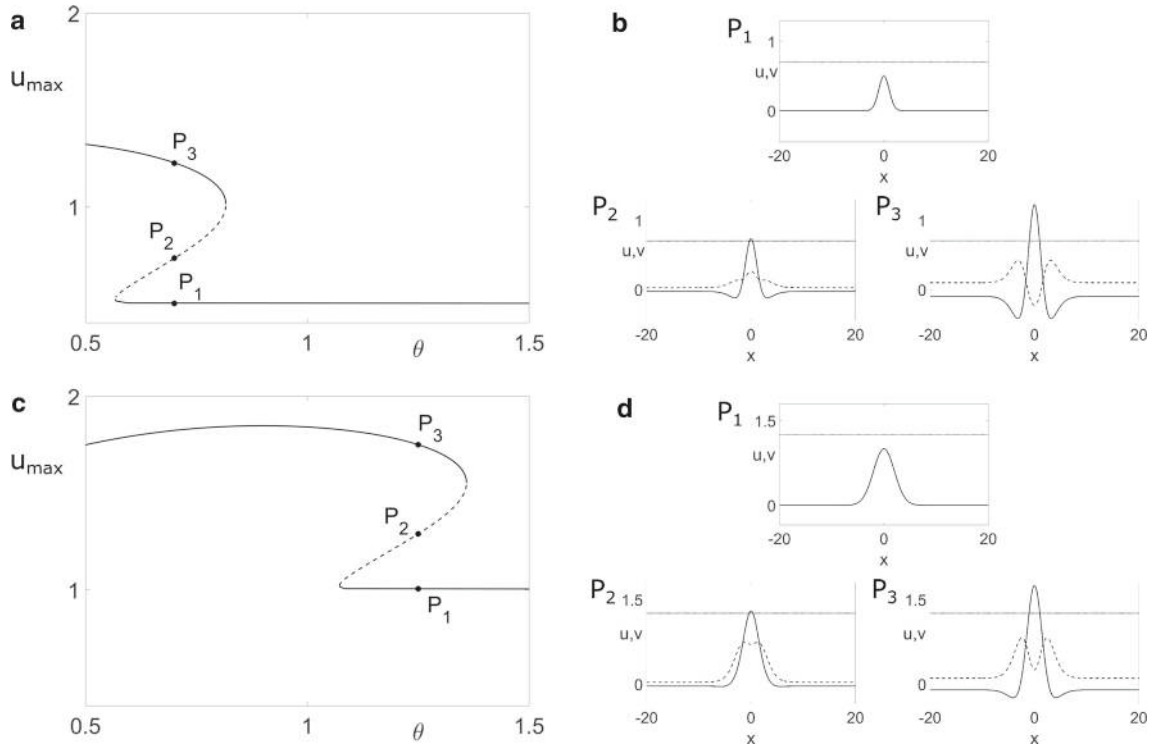

Fig. 4 **a** and **c** Bifurcation curves showing one-bump solutions of (1) with the initial condition (22) with $A_K = 1$, $\sigma_K = 1$ (**a**) and $A_K = 2$, $\sigma_K = 2$ (**c**) as the parameter θ is varied. Solid (dashed) lines represent stable (unstable) solutions. Examples of solutions at the points P_1, P_3 (stable) and P_2 (unstable) for a narrower and a wider profile of $K(x)$ are shown in panels (**b**) and (**d**), respectively. Threshold $\theta = 0.7$ (**b**) and $\theta = 1.25$ (**d**) (dotted line). Parameters of the kernel as in Fig. 2

parameters, Fig. 6 depicts the bifurcation curve when the lateral inhibition parameter σ_{inh} is varied. As illustrated by the two pairs of stable and unstable two-bumps, (P2, P3) and (P1, P4), respectively, the distance decreases with increasing σ_{inh}. The Amari model would predict for the same distances a pronounced repulsive interaction of the two localized activation patterns.

3.3.2 Existence and stability of N-bump solutions

It is well known that classical continuous attractor networks have difficulties simultaneously stabilizing multiple bumps due to the constraints imposed by lateral inhibition and the interference between nearby patterns (Amari 1977; Wei et al. 2012). This limitation has been addressed in computational studies by introducing additional processing mechanism such as short-term synaptic facilitation (Rolls et al. 2013) or by using interaction kernels that are not of lateral-inhibition type (Ferreira et al. 2016; Laing and Troy 2003). However, already Amari (1980) pointed out that for the connectivity function (2) multiple stable bumps may exist at distances, $|x| > x_c$, where the lateral inhibition is spatially uniform (for multi-item WM applications see e.g. Johnson et al. 2009; Wei et al. 2012).

It is straightforward to derive a condition for the existence of an N-bump which is constrained by the summed inhibition that each bump receives from the $N-1$ neighboring patterns. The bump width depends on N but should be equal for each bump. For the numerical realization in a finite integration domain, one has to apply circular boundary conditions or open boundary conditions with a sufficiently wide lateral inhibition kernel. Without loss of generality, we assume that the bump is located in the interval $[-\Delta/2, \Delta/2]$ and that the remaining $N-1$ pulses are located in the intervals $[x_1 - \Delta/2, x_1 + \Delta/2]$, $[x_2 - \Delta/2, x_2 + \Delta/2]$, …, $\left[x_{N-1} - \Delta/2, x_{N-1} + \Delta/2\right]$, with $x_{i+1} - x_i > \Delta + x_s$, $i = 1, 2, \ldots, N-1$. That is, $u(x) > \theta$ for $x \in [-\Delta/2, \Delta/2] \cup [x_1 - \Delta/2, x_1 + \Delta/2] \cup \ldots \cup \left[x_{N-1} - \Delta/2, x_{N-1} + \Delta/2\right]$, and $u(x) \leq \theta$ elsewhere.

Equilibrium solutions of the two-population model are given by

$$U(x) = V(x) + \int_{-\Delta/2}^{\Delta/2} w(y)\mathrm{d}y + \int_{x_1-\Delta/2}^{x_1+\Delta/2} w(y)\mathrm{d}y + \ldots + \int_{x_{N-1}-\Delta/2}^{x_{N-1}+\Delta/2} w(y)\mathrm{d}y, \tag{23a}$$

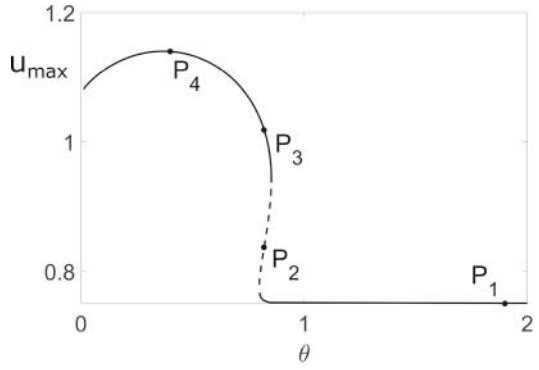

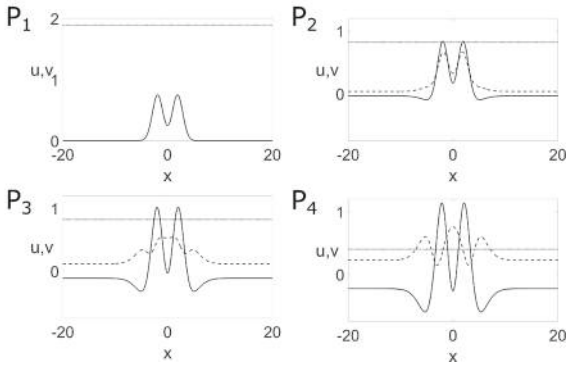

Fig. 5 Bifurcation curve showing two-bump solutions of (1) with the initial condition (22) with $A_K = 1.5$, $\sigma_K = 1$ as the parameter θ is varied. Solid (dashed) lines represent stable (unstable) solutions. Examples of two-bump solutions at the points P_1, P_3, P_4 (stable) and P_2 (unstable) are shown. Threshold θ (dotted line): $\theta = 1.9$ (P_1), $\theta = 0.82$ (P_2 and P_3), $\theta = 0.4$ (P_4). Parameters of the kernel as in Fig. 2

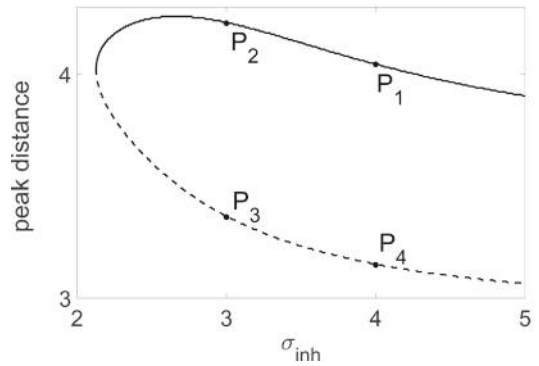

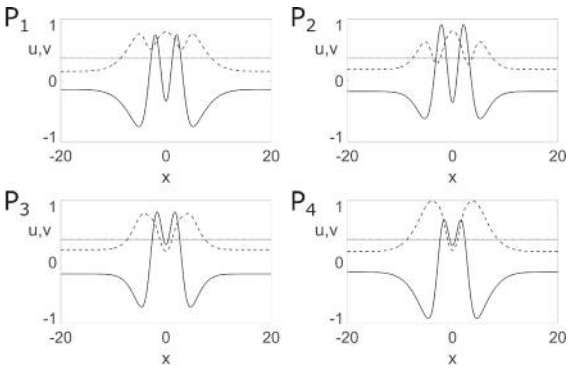

Fig. 6 Bifurcation curve showing two-bump solutions of (1) with the initial condition (22) with $A_K = 1.5$, $\sigma_K = 1$ as the parameter σ_{inh} is varied. Solid (dashed) lines represent stable (unstable) solutions. Examples of two-bump solutions at the points P_1, P_2 (stable) and P_3, P_4 (unstable) are shown. $\sigma_{inh} = 3$ (P_2 and P_3), $\sigma_{inh} = 4$ (P_1 and P_4). Remaining parameters as in Fig. 2

$$V(x) = U(x) - \int_{-\Delta/2}^{\Delta/2} w(y)\mathrm{d}y - \int_{x_1-\Delta/2}^{x_1+\Delta/2} w(y)\mathrm{d}y - \ldots - \int_{x_{N-1}-\Delta/2}^{x_{N-1}+\Delta/2} w(y)\mathrm{d}y. \tag{23b}$$

Since at the boundaries of a bump $U(-\Delta/2) = U(\Delta/2) = \theta$, $U(x) + V(x) = K$ and

$$\int_{x_i-\Delta/2}^{x_i+\Delta/2} w(y)\mathrm{d}y = -\Delta w_{inh}, \tag{24}$$

we get the existence condition for N-bump solutions

$$F(\Delta) = -2\theta + K + W(\Delta) - (N-1)\Delta\, w_{inh} = 0. \tag{25}$$

The width of an individual bump of an N-bump solution can be thus found graphically by looking on the intersection of the plot of $W(\Delta)$ with the line $2\theta - K + (N-1)\Delta w_{inh}$. Figure 7 shows an example for the case $K = 2\theta$ and $N = 2$. The maximum number of stable bumps that the specific connection function supports is $N = 6$. A further increase of lateral inhibition would destabilizes the bumps since $\mathrm{d}W(\Delta)/\mathrm{d}\Delta > 0$. The analogous condition for the existence of an N-bump solution in the Amari model is given by

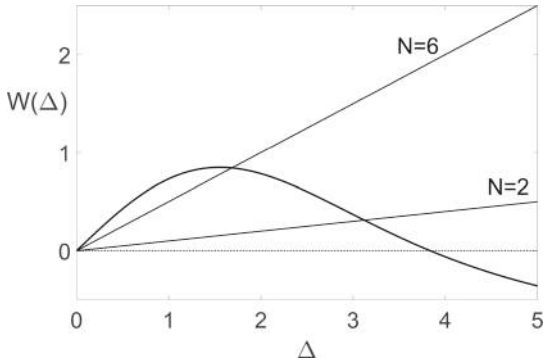

Fig. 7 Existence of N one-bump solutions in the two-field model with the Mexican-hat kernel (2). Threshold $\theta = 0.5$ and $K = 1$. Straight lines show the condition (25) for $N = 2$ and $N = 6$. Parameters of the kernel as in Fig. 2

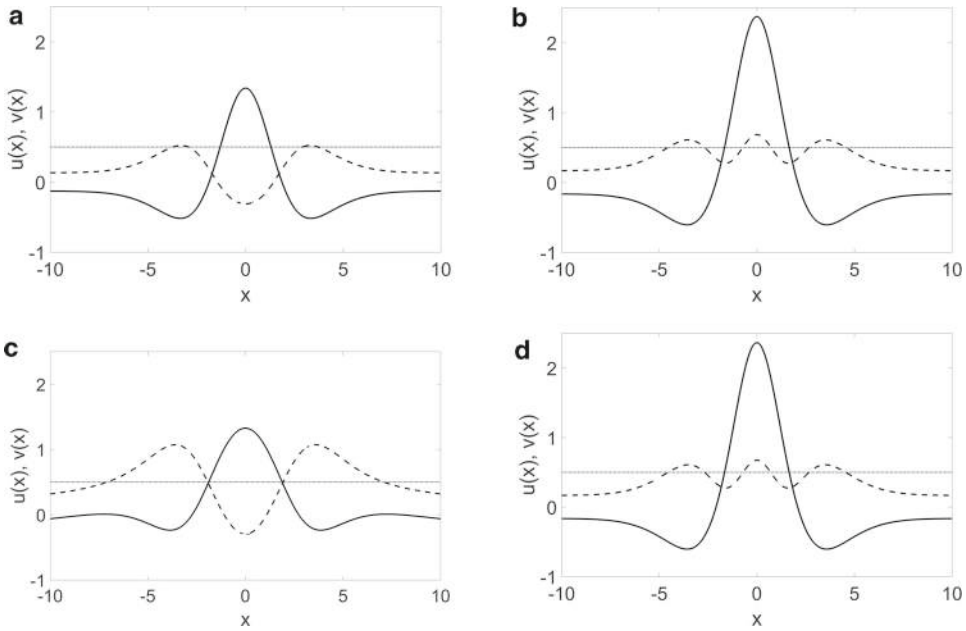

Fig. 8 Solutions at time $t = 50$ of the model (1) created with transient inputs $I(x, t)$ given by (3) with variation of (**b**) input strength A_I, (**c**) input width σ_I and (**d**) input duration d_I. Parameters of the inputs: (**a**) $A_{I_1} = 1, \sigma_{I_1} = 1, d_I = 1$ (**b**) $A_{I_1} = 3, \sigma_{I_1} = 1, d_I = 1$ (**c**) $A_{I_1} = 1, \sigma_{I_1} = 6, d_I = 1$ (**d**) $A_{I_1} = 1, \sigma_{I_1} = 1, d_I = 3$. The kernel w is given by (2) with $A_{ex} = 2$, $A_{in} = 1$, $\sigma_{ex} = 1.25$, $\sigma_{in} = 2.5$ and $w_{inh} = 0.1$. Threshold $\theta = 0.5$ (dotted line), $K = 0$

$$F(\Delta) = -\theta + W(\Delta) - (N-1)\Delta\, w_{inh} = 0. \tag{26}$$

For the example of Fig. 7, the maximum number of bumps reduces in this case to $N = 3$. In the next section we show that different to the Amari model with Mexican-hat connectivity, the two-field model supports multi-bump solutions created by inputs at any distance.

4 Input driven bump solutions

In working memory applications, classical bump attractor models implement the encoding and maintenance of briefly presented visual input as an all-or-none process. The information is either stored in a self-stabilized bump with a shape defined by the recurrent interactions or the information is completely lost since neural activity decays back to resting state. However, a growing body of experimental evidence indicates that this binary classification may be insufficient as a description of WM storage, because the representational quality of WM items may differ depending on sensory attributes of the input or task demands. For instance, the salience of the visual input manipulated through varying stimulus strength (or contrast) is known to affect WM representations. Consistent with the notion of memory-associated persistent activity, a graded modulation of sustained population activity as a function of stimulus contrast has been described in a WM task (Constantinidis et al. 2001).

Figure 8 shows various bump solutions of the two-field integrator model in which input attributes are systematically varied. In panels (a) and (b), the attractor network converts a transient input into a persistent output which is proportional to the input amplitude. A comparison of panels (a) and (c) illustrates that the bump also represents faithfully input width. This property can be exploited for instance to encode uncertainty in the sense of an explicit probability code (Ma and Jazayeri 2014). Higher uncertainty is then represented by a wider activation pattern across the neural population tuned to a continuous input feature (e.g., representing ranges of movement direction (Erlhagen and Schöner 2002)). In panel (d), the localized input of panel (a) is applied but lasting three times as long. The amplitude of the evolving bump equals the bump amplitude in panel (b), as expected by perfect integration. The two-field model can thus be used to model the encoding of input duration (Wojtak et al. 2019) if one assumes that the input amplitude is first normalized by upstream sensory processing (Carandini and Heeger 2012).

Figure 9 shows the temporal evolution of a bump in two dynamic input scenarios which can be expected in any natural environment. In the first example (a), the strength of evidence continuously increases during the stimulation period. The bump amplitude reflects again the total external input applied to the population. The observed ramping-like activity is a hallmark of "drift-diffusion" models of decision making which assume the continuous accumulation of sensory and other evidence to a threshold (for review see Bogacz 2007). To investigate the dependence of the bump shape on input width, a truncated Gaussian input ($I(x, t) = 0,\ |x| > 1.5\sigma$) has been applied. As can be seen in panel (b), the bump width reaches its maximum well before the end of the stimulation period. For a read-out of the population activity by a downstream network this means that a gain in certainty about the most likely parameter value as expressed in the bump amplitude is not necessarily accompanied by more uncertainty

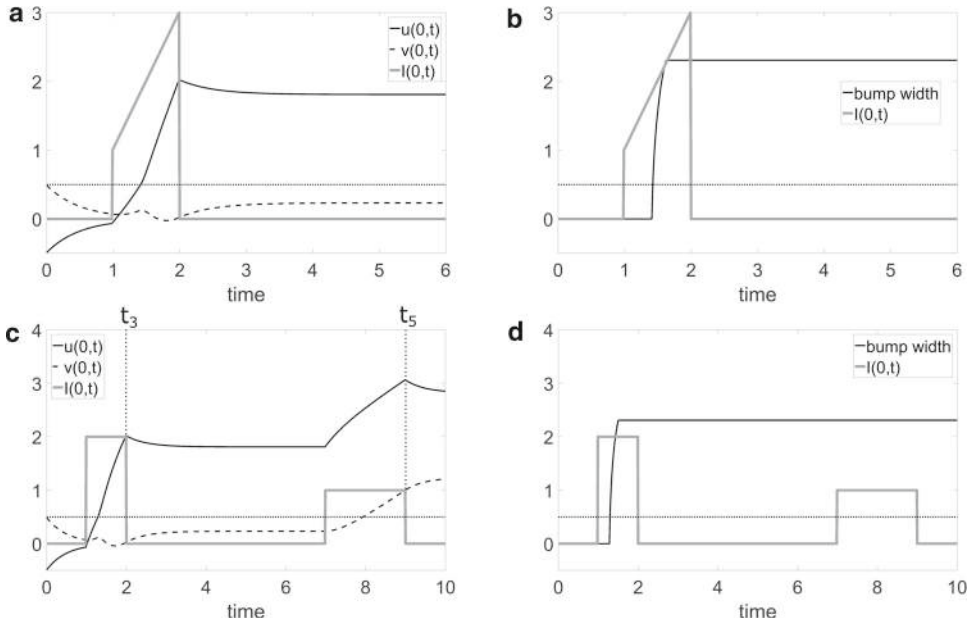

Fig. 9 The temporal evolution of the bump amplitude and the bump width is shown for a dynamic input with continuously increasing strength and constant width (**a** and **b**), and for two sequentially presented inputs with constant amplitude and width (**c** and **d**). A truncated Gaussian with standard deviation $\sigma = 1$ and $I(x,t) = 0$ for $|x| > 1.5\sigma$ is applied: (**a**) $A_{I_1} = [1, 3]$, $d_I = 1$; (**c**) first input $A_{I_1} = 2$, $d_I = 1$, second input $A_{I_1} = 1$, $d_I = 2$. The kernel w is given by (2) with $A_{ex} = 2$, $A_{in} = 1$, $\sigma_{ex} = 1.25$, $\sigma_{in} = 2.5$ and $w_{inh} = 0.1$. Threshold $\theta = 0.5$ (dotted line), $K = 0$

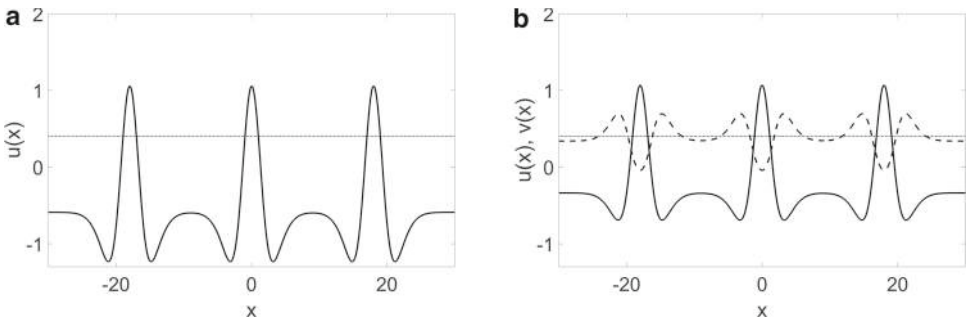

Fig. 10 Solutions of the Amari model (**a**) and the two-field model (**b**) at time $t = 50$ created with simultaneous inputs. Input $I(x,t)$ with $A_{I_{1,2,3}} = 1, \sigma_{I_{1,2,3}} = 1, d_I = 1$ is applied at time $t = 1$ at positions $x_{c_{1,2,3}} \in \{-18, 0, 18\}$. The kernel w is given by (2) with $A_{ex} = 2$, $A_{in} = 1$, $\sigma_{ex} = 1.25$, $\sigma_{in} = 2.5$ and $w_{inh} = 0.1$. Threshold $\theta = 0.4$ (dotted line), $K = 0$

about the range of possible parameter values as expressed by a broadening of the activity distribution. To work as a robust neural integrator over a longer timescale of a decision process, the network dynamics should hold the activity level without significant decay or growth when an input signal vanishes. In the second example (c), the localized input is applied sequentially with different strength at the same field site $x = 0$. As can be seen in the time evolution plot, the population activity stabilizes at a constant level after input cessation at times t_3 and t_5, respectively. Panel (d) illustrates that the bump width established during the first stimulation period does not change when the second input is applied.

The existence of stable multi-bump solutions discussed in Sect. 3 does not necessarily mean that their evolution can be triggered by external inputs. In field models of lateral inhibition type, any existing suprathreshold activity will amplify the competitive effect of the fast inhibitory feedback. This means that in order to create an input-driven multi-bump, no processing advantage should be given to a specific subpopulation in terms of the timing and the strength of the input. For the two-field model, the competitive effect of lateral inhibition is predicted to be counterbalanced to some extent since the spatial integration of the v-population with an inverted Mexican hat profile propagates excitation outwards from stimulated regions. Figure 10 shows that in both models, three bumps evolve when three identical, transient inputs are applied at the same time. The situation is different for a sequential stimulation protocol (Fig. 11). In the Amari case, only the first input triggers the evolution of a bump whereas the locally balanced dynamics of the two-field model stabilizes again three bumps. It is worth noting that suppression effects due to lateral inhibition can be also observed in the two-field model. In the next section we show that when inputs with different amplitudes are applied, the bump representation of a weaker input may become suppressed below threshold.

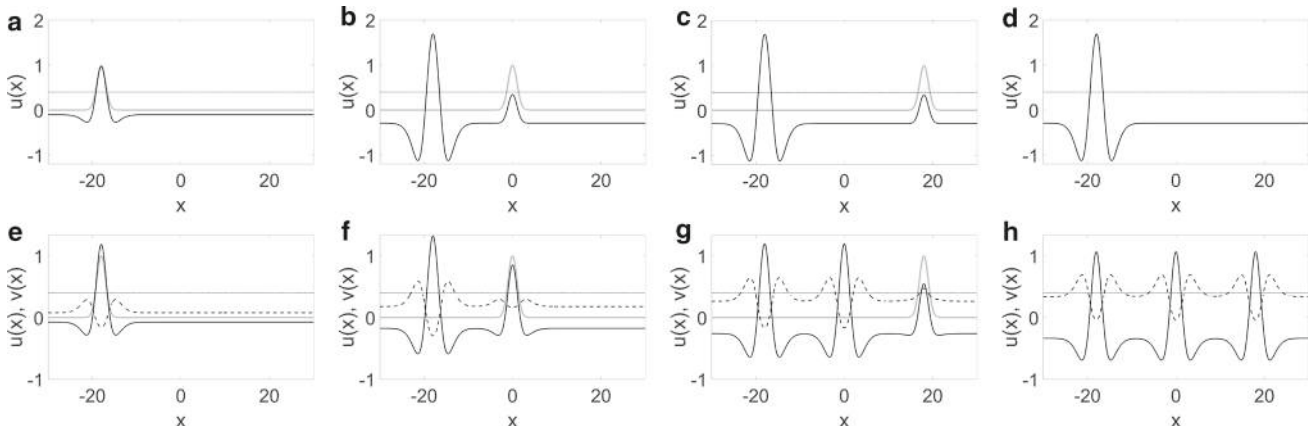

Fig. 11 Solutions of the Amari model (**a**–**d**) and the two-field model (**e**–**h**) created with sequential inputs. Inputs $I(x,t)$ (gray lines) are applied at times $t_1 = 1, t_2 = 10$ and $t_3 = 20$ at positions $x_{c_{1,2,3}} \in \{-18, 0, 18\}$. Snapshots taken at times: $t = 2$ (**a** and **e**), $t = 11$ (**b** and **f**), $t = 21$ (**c** and **g**), $t = 50$ (**d** and **h**). The parameters for all three sequential inputs are $A_{I_1} = 1, \sigma_{I_1} = 1, d_I = 1$. Parameters of the kernel as in Fig. 10. Threshold $\theta = 0.4$ (dotted line), $K = 0$

4.1 Retro- cueing task

The representational quality of WM items is not only shaped by bottom-up input features as discussed above but may be also modulated by top-down signals representing task demands (Wildegger et al. 2016). A behavioral paradigm that has attracted considerable interest over the last decade is retro- cueing (for an overview see Souza and Oberauer 2016). It shows that memory performance can be enhanced by a cue indicating the most relevant item for the current task goals, even when the cue is applied long after the input array has been removed. A simple application of prioritizing an item during WM maintenance is a task in which the spatial location of two equally task-relevant movement targets has to be memorized, the information about the location to visit first may vary and becomes available only later during the task. The exact mechanisms underlying the retro-cueing benefit are still debated but recent modeling and experimental work suggests that top-down signals generate neural contrast by enhancing the neural population representations of the cued item and inhibiting activity of items irrelevant to current task goals (Bays and Taylor 2018; Gazzaley and Nobre 2012). As illustrated in Fig. 12, this view is consistent with the dynamics of the integrator model when a second transient input is applied to one of the two fields sites that had already developed a bump in response to a first input. In the context of the mentioned application, it is interesting to note that a neural activation gradient is the hallmark of so-called competitive cueing models of serial order (Rhodes et al. 2004). In dynamic field implementations of this model class, a competitive winner-take-all dynamics in a decision field, which receives the memory gradient as input, is used to recall the stored serial order (Ferreira et al. 2020).

Recent findings in functional magnetic resonance imaging (fMRI) studies using a retro-cueing paradigm have challenged the assumption that multiple items can be concurrently represented in an active state of persistent neural activity (Rose et al. 2016; Sprague et al. 2016). The findings have been interpreted as evidence that only the currently most task-relevant item is maintained in a persistent state whereas the memories of currently unattended items are stored in stimulus-selective patterns of short-term synaptic facilitation. Computational models show that such latent "activity-silent" memory traces in the neural network can be restored into an active state by retro-cues or other non-specific read-out signals (Mongillo et al. 2008; Trübutschek et al. 2017). However, the findings of the neurophysiological experiments are not conclusive since the applied data analysis technique might not be sensitive enough to detect the signatures of weak sustained neural activity associated with unattended items (Masse et al. 2020, see Sutterer et al. 2019 for neural evidence of multiple active WM representations). In fact, a recent modeling study based on the dynamic neural field framework convincingly showed that all key experimental findings of the fMRI retro-cue study (Sprague et al. 2016) could be reproduced relying entirely on sustained neural activity for WM representations (Schneegans and Bays 2017). The existence of subthreshold bumps in the two-field model supports the notion that also weak population activity can be sustained over behaviorally relevant timescales. Figures 13a and 13b show simulations of the same retro-cue task as in Figure 12 but with weaker initial inputs and stronger cue. The field develops again two bumps but with a closer to threshold activation level. The main difference is that the population representation of the item without cue now appears to be suppressed below threshold. Figure 13c shows that like

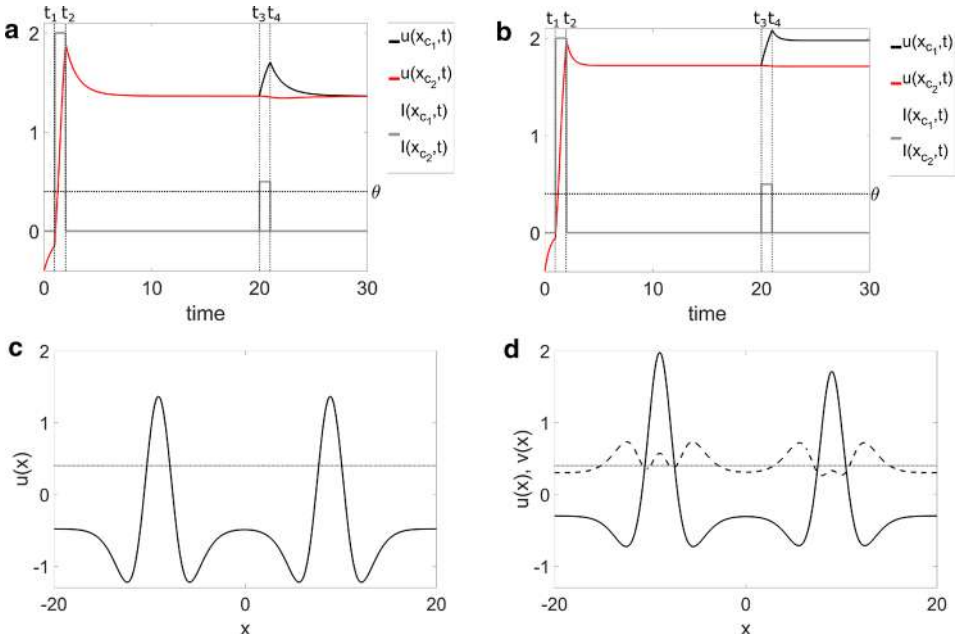

Fig. 12 Retro- cueing task in the Amari model (**a** and **c**) and in the two-field model (**b** and **d**). Bumps are created with two inputs (grey lines) with $A_{I_{1,2}} = 2, \sigma_{I_{1,2}} = 1, d_I = 1$ applied simultaneously at time $t_1 = 1$ at positions $x_{c_1} = -9$ and $x_{c_2} = 9$. At a later time $t_3 = 20$, an additional weak input with $A_{I_1} = 0.5, \sigma_{I_1} = 1, d_I = 1$ is applied to one of the memories at x_{c_1}. (**a** and **b**) Temporal evolution of activity at sites x_{c_1} (black lines) and x_{c_2} (red lines) in both models. (**c** and **d**) Snapshots showing the final solutions at time $t = 50$. The kernel w is given by (2) with $A_{ex} = 2$, $A_{in} = 1$, $\sigma_{ex} = 1.25$, $\sigma_{in} = 2.5$ and $w_{inh} = 0.1$. Threshold $\theta = 0.4$ (dotted line), $K = 0$

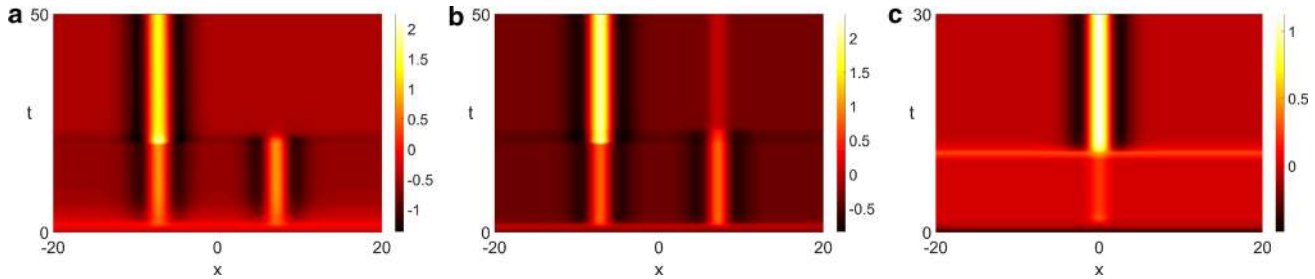

Fig. 13 (**a** and **b**) Retro-cueing task in the Amari model (**a**) and in the two-field model (**b**). Bumps were initially created with two inputs with $A_{I_{1,2}} = 0.75, \sigma_{I_{1,2}} = 1, d_I = 1$. Later at time $t = 20$ an additional input with $A_{I_1} = 2, \sigma_{I_1} = 1, d_I = 1$ was applied to one of the memories. The kernel w is given by (2) with $A_{ex} = 2$, $A_{in} = 1$, $\sigma_{ex} = 1.25$, $\sigma_{in} = 2.5$ and $w_{inh} = 0.2$. Threshold $\theta = 0.4$, $K = 0$. (**c**) Recovery of a "forgotten memory" in the two-field model using unspecific input. A subthreshold bump is first created with an input with amplitude $A_{I_1} = 0.45 < \theta$ and $\sigma_{I_1} = 1$ applied at time $t = 1$ for duration $d_I = 1$. A spatially constant input $I(x) = 0.4$ is applied at time $t = 10$ for the duration $d_I = 1$. Parameters of the kernel as in panels (**a** and **b**). $K = 0, \theta = 0.5$

in the computational studies of the activity-silent WM mechanism, the application of an unspecific input signal that does not provide any spatial information is sufficient to restore a subthreshold memory trace into a suprathreshold activity pattern.

4.2 Interacting bumps

An attractive feature of continuous attractor models is that they accurately explain errors in WM and other behavioral tasks as a distance-dependent interaction between two or more neural population representations (Almeida et al. 2015; Erlhagen et al. 1999; Johnson et al. 2009; Wilimzig et al. 2006). DNF models with Mexican-hat connectivity predict that when two transient inputs are presented in close proximity, the network dynamics exhibits an attraction effect (Amari 1977; Krishnan et al. 2018). As shown in Figure 14, the Amari model makes the strong prediction that there is no possibility to independently store very similar points of a continuous feature dimension since the two initially disjoint activity patterns will completely merge. This attraction effect has been exploited for instance to model target

selection of fast saccadic eye movements that are known to land between two close targets ("averaging saccade" Wilimzig et al. 2006). However, the finding in a WM task of no performance impairment when items in memory are similar has challenged the generality of the averaging hypothesis of simultaneously processed nearby feature values (Lin and Luck 2009). The two-field model develops in response to the same transient inputs a broad activation pattern with two peaks which is clearly distinguishable from a one-bump solution triggered by a single input. Interestingly, a recent experiment investigating a possible neural substrate of saccadic averaging in the superior colliculus (SC) reports that the simultaneous stimulation of two nearby SC sites evokes a single merged activation pattern centered between the two sites (Vokoun et al. 2014). Consistent with the prediction of the two-field model, the spread of activation appears to be significantly wider than the localized activity pattern induced by a single stimulation. In WM applications, a downstream read-out mechanism might interpret the existence of the two peaks and the relatively suppressed activity at the intermediate position as evidence for the storage of two similar inputs (Lin and Luck 2009). An attraction effect still manifests since the peak distance is smaller than the original input distance (Almeida et al. 2015).

For intermediate input distances, the gradient in the lateral inhibition profile causes the peaks of activity to shift away from each other. Direct neurophysiological evidence for such a repulsion effect has been reported (Erlhagen et al. 1999; Jancke et al. 1999) and the finding of a repulsive bias in some behavioral experiments is in good agreement with the qualitative model prediction (Almeida et al. 2015; Johnson et al. 2009; Wang et al. 2012). However, the predicted size of the repulsion effect differs significantly for the Amari and the two-field models. The two transient inputs, which in the example shown in Figure 15 overlap to some extent, set the dynamics of the two-field model in the basin of attraction of a two-bump solution with an inter-peak distance larger than the input distance. In the Amari case, the attractor state represents two individual bumps located at a further increased distance for which the mutually inhibitory interaction is spatially uniform. As shown in Fig. 6, the magnitude of the repulsive bias can be controlled by the parameter σ_{inh}.

A third type of a distance-dependent interaction effect discussed in continuous attractor models is bump annihilation (Krishnan et al. 2018; Wei et al. 2012). It may occur when a bump is closely flanked by two others. Figure 16a shows an example of the Amari model where the summed lateral inhibition of the two flanking bumps suppresses the input-induced suprathreshold activity at the intermediate position $x = 0$, resulting in a complete memory loss. Bump annihilation thus limits the number of items that can be simultaneously stored in a field of a given size. The situation is different for the integrator model where the same input pattern develops three bumps (b). Since the middle bump at $x = 0$ has a slightly smaller width and amplitude, it shows that the bump shape can be affected by the existence of nearby activity patterns. Note that with increasing input distance, this inhibition effect would diminish and finally disappear completely, leading to a memory representation of three independent locations (not shown). With inputs closer to the threshold, the middle bump becomes suppressed below the threshold but the activity still remains sustained (c). Recent experimental findings support the notion of a neural encoding and maintenance of weak visual inputs into WM that do not reach the threshold for conscious perception but may still affect goal-directed behavior (Soto et al. 2011). Models of capacity limits of working memory are silent on this issue (Trübutschek et al. 2017). Future research might attempt to more directly test the hypothesis that sustained subthreshold activity constitutes a neural substrate of conscious or unconscious memory.

4.3 Bump drift and bump interaction in the stochastic integrator model

To evaluate the impact of random fluctuations on the evolution and maintenance of input-driven bumps of the two-field model, we use a stochastic version of the field equations with additive noise. It is given by

$$\frac{\partial u(x,t)}{\partial t} = -u(x,t) + v(x,t) + I(x,t) + \epsilon^{1/2} \mathrm{d}W(x,t) + \int_\Omega w(|x-y|) f(u(y,t)-\theta) \mathrm{d}y, \tag{27a}$$

$$\tau_v \frac{\partial v(x,t)}{\partial t} = -v(x,t) + u(x,t) - \int_\Omega w(|x-y|) f(u(y,t)-\theta) \mathrm{d}y, \tag{27b}$$

where $\mathrm{d}W(x,t)$ is the increment of a spatially correlated Wiener process such that

$$\langle \mathrm{d}W(x,t) \rangle = 0, \tag{28}$$

$$\langle \mathrm{d}W(x,t) \mathrm{d}W(y,s) \rangle = C(x-y)\delta(t-s)\mathrm{d}t\mathrm{d}s, \tag{29}$$

and $\epsilon \ll 1$ is the noise amplitude.

Closely following the conceptually related bump attractor model of Carroll and colleagues (Carroll et al. 2014), we choose a cosine spatial correlation function

$$C(x) = \pi \cos(x). \tag{30}$$

The correlation function $C(x-y)$ can be related directly to a spatial filter $\mathcal{F}(x-y)$. The term $\mathrm{d}W(x,t)$ can be defined by convolving a spatially white noise process $\mathrm{d}\mathcal{Y}(x,t)$, satisfying $\langle \mathrm{d}\mathcal{Y}(x,t) \rangle = 0$ and $\langle \mathrm{d}\mathcal{Y}(x,t) \mathrm{d}\mathcal{Y}(y,s) \rangle = \delta(x-y)\delta(t-$

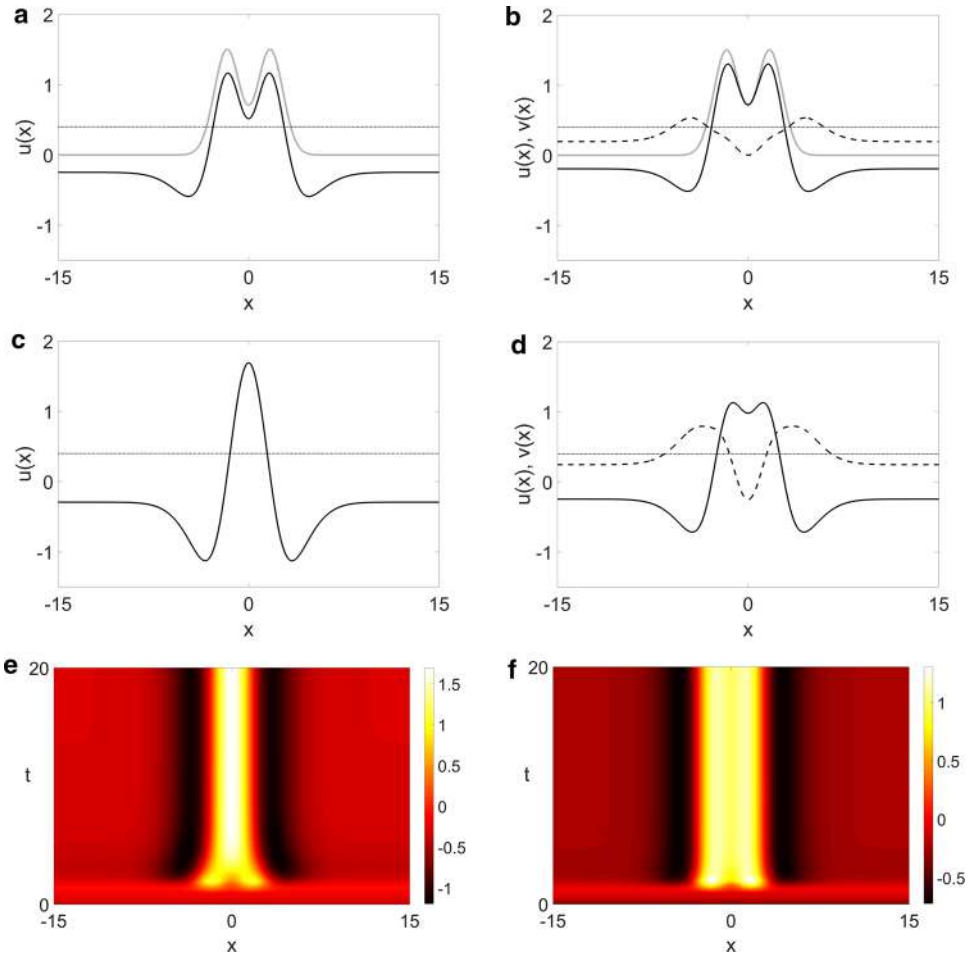

Fig. 14 Merging bumps in the Amari model (left column) and in the two-field model (right column). Bumps created with two inputs with $A_{I_{1,2}} = 1.5$, $\sigma_{I_{1,2}} = 1$, $d_I = 1$, applied at time $t = 1$ at positions $x_{c_{1,2}} = \pm 1.7$. (**a** and **b**) Snapshots at time $t = 2$ when input (gray lines) is still present. (**c** and **d**) Steady states at time $t = 50$. (**e** and **f**) Space-time plot of field activity. The kernel w is given by (2) with $A_{ex} = 2$, $A_{in} = 1$, $\sigma_{ex} = 1.25$, $\sigma_{in} = 2.5$ and $w_{inh} = 0.1$. Threshold $\theta = 0.4$ (dotted line), $K = 0$

$s)\mathrm{d}t\mathrm{d}s$ with the filter $\mathcal{F}(x - y)$ such that

$$\mathrm{d}W(x,t) = \int_{\Omega} \mathcal{F}(x-y)\mathrm{d}\mathcal{Y}(y,t)\mathrm{d}y, \tag{31}$$

where $\mathcal{F}(x - y) = C(x - y)$. The noise term is added to the u-equation only. This allows us to directly compare the simulations of the two-field model with the behavior of the Amari model. Our simulations show that adding the same noise model also to the v-equation does not change the qualitative model predictions reported here.

4.3.1 Bump drift

Due to the neutral stability of a bump in a continuous attractor network, random noise may lead to a drift of the bump in the absence of tuned external input (Camperi and Wang 1998; Carroll et al. 2014; Kilpatrick and Ermentrout 2013). Stochastic dynamic field models thus predict a time-dependent loss of precision of WM representations. Direct neurophysiological and behavioral evidence for this prediction comes from a recent study using a spatial WM paradigm in which a monkey had to make saccadic eye movements to a remembered target. The results showed that the recalled location deviates on a trial-by-trial basis precisely in the direction of the drift of the tuned population activity at the end of the delay period (Wimmer et al. 2014).

Figure 17 shows for a single run of the stochastic integrator the bump drift at a fixed time (a) and in a space-time plot (b). Larger drifts represent larger errors of the memorized location relative to the location represented by the neural activity during input presentation at time $t = 0$ at position $x = 0$. Since recall precision is known to be influenced by bottom-up sensory salience and top-down factors like retro-cues, the bump amplitude representing the quality or strength of the item memory should affect the drift rate (Carroll et al. 2014). We tested this prediction in simulations of the stochastic model with inputs of varying strength (100 simulations for each strength). As shown in panel (c), the variance of the bump center position decreases systematically with increasing bump amplitude. For the highest amplitude tested, the fluctuations over time around the true input position are rather small. This dependence of the drift on memory strength replicates the results obtained with the DNF model proposed by Carroll and Kilpatrick (Carroll et al. 2014). Since there is

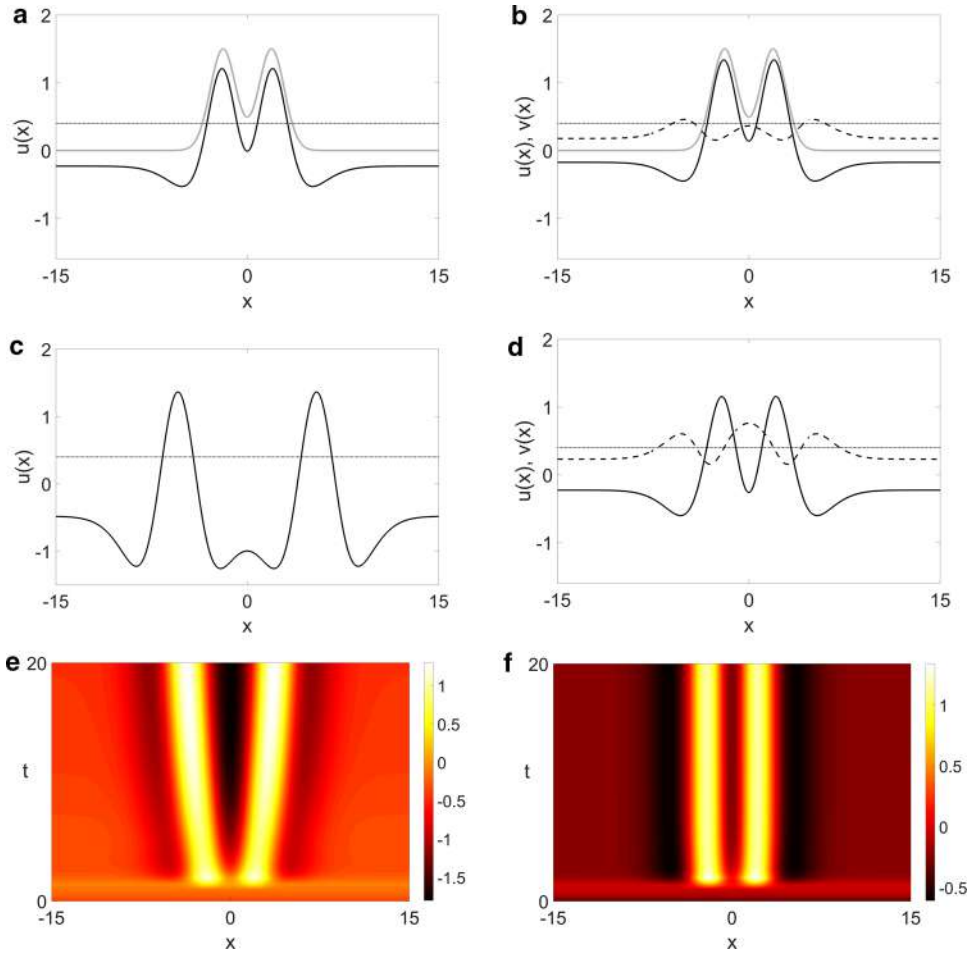

Fig. 15 Repulsive bumps in the Amari model (left column) and in the two-field model (right column). Bumps created with two inputs with $A_{I_{1,2}} = 1.5$, $\sigma_{I_{1,2}} = 1$, $d_I = 1$, applied at time $t = 1$ at positions $x_{c_{1,2}} = \pm 1.9$. (**a** and **b**) Snapshots at time $t = 2$ when input (gray lines) is still present. (**c** and **d**) Steady states at time $t = 200$. (**e** and **f**) Space-time plots of field activity. The kernel w is given by (2) with $A_{ex} = 2$, $A_{in} = 1$, $\sigma_{ex} = 1.25$, $\sigma_{in} = 2.5$ and $w_{inh} = 0.1$. Threshold $\theta = 0.4$ (dotted line), $K = 0$. The solution in panel **d** is solution P_4 shown in Fig. 5

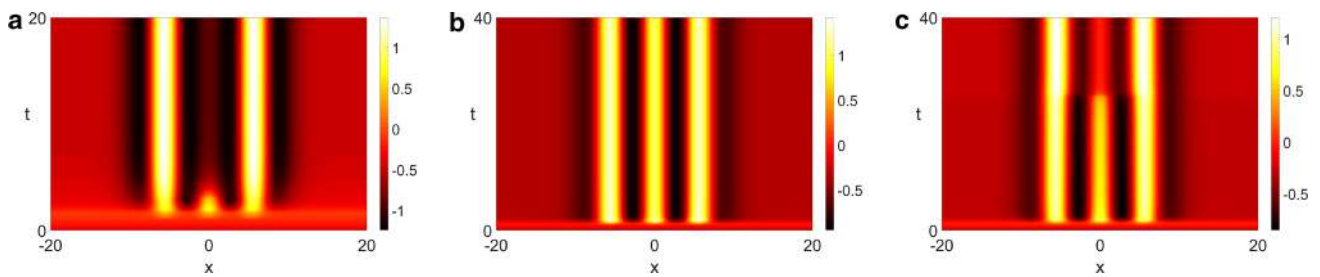

Fig. 16 Space-time plots of field activity in the Amari model (**a**) and the two-field model (**b** and **c**). (**a**) Bump annihilation in the Amari model. Bumps created with three inputs with $A_{I_{1,2,3}} = 1$, $\sigma_{I_{1,2,3}} = 1$, $d_I = 1$, applied at time $t = 1$ at positions $x_{c_{1,2,3}} \in \{-5.5, 0, 5.5\}$. (**b** and **c**) Three-bump solutions of the two-field model. Bumps created with three inputs with $A_{I_{1,2,3}} = 1.5$ (**b**) and $A_{I_{1,2,3}} = 1$ (**c**) applied at time $t = 1$ at positions $x_{c_{1,2,3}} \in \{-5.5, 0, 5.5\}$. Remaining input parameters $\sigma_{I_{1,2,3}} = 1, d_I = 1$. The kernel w is given by (2) with $A_{ex} = 2, A_{in} = 1$, $\sigma_{ex} = 1.25$, $\sigma_{in} = 2.5$ and $w_{inh} = 0.2$. Threshold $\theta = 0.4$, $K = 0$

no dependence of bump shape on input features in the Amari model, there is a unique drift pattern. For the present parameter setting, it is comparable with the pattern observed with input strength $A_I = 3$ of the two-field model.

4.3.2 Bump interaction

As shown in section 4.2, recall precision in continuous attractor models also depends on potential interference of nearby memory traces. We have therefore tested the behavior of the stochastic integrator model with two simultaneously presented inputs. They were placed at a critical distance where in the deterministic case a repulsion effect manifests and

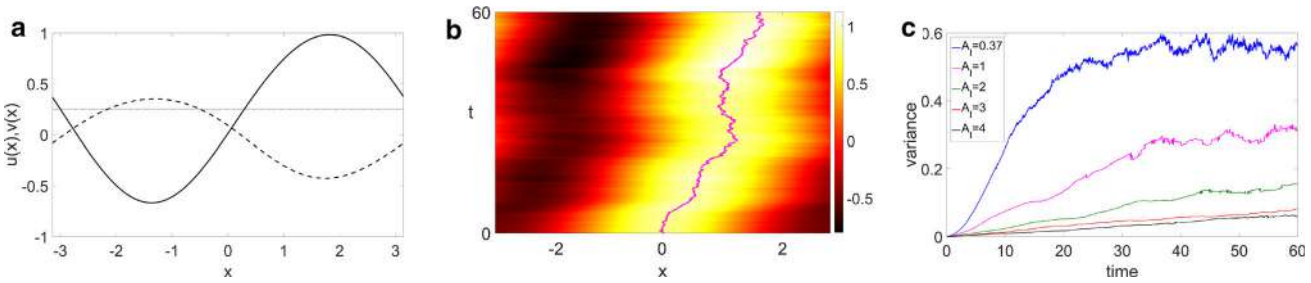

Fig. 17 Bump diffusion in the stochastic two-field model. (**a**) Bump solution at time $t = 60$. The initial condition is a bump centered at $x = 0$. (**b**) Space-time plot showing the bump drift. The magenta line indicates the bump center. (**c**) Variance of bump position computed for $N = 100$ numerical simulations of the model with different input strengths A_I. Remaining input parameters $\sigma_{I_1} = 1$, $d_I = 1$. The kernel w is given by (2) with $A_{ex} = 2$, $A_{in} = 1$, $\sigma_{ex} = 1.5$, $\sigma_{in} = 2.5$ and $w_{inh} = 0.3$. Threshold $\theta = 0.25$ (dotted line in panel (**a**)), $K = 0$, $\epsilon = 0.005$, $L = \pi$. The spatial and temporal resolution is $\mathrm{d}x = 0.01$ and $\mathrm{d}t = 0.01$, respectively

a small reduction of the input distance ($2\,\mathrm{d}x$, where $\mathrm{d}x$ is the numerical mesh size) causes attraction (Almeida et al. 2015). Figure 18 (a) shows overlaid activity profiles of an evolving two-bump solution taken at a fixed time in different model simulations. As can be clearly seen, the additive noise causes a switching between either attraction or repulsion in different trials. Panel (b) shows that the magnitude of the interference effect appears to be greatly reduced when stronger inputs are applied. Panel (c) shows this dependence on input strength/bump amplitude in a more quantitative manner by plotting the variance of the inter-peak distance as a function of time. To allow a direct comparison, Figure 19 depicts, for the same input distance, the activity pattern at a fixed time in two runs of the stochastic Amari model. It develops either a single bump (a) or two bumps with repulsion (b). The model simulations reveal that the single bump may be the result of a suppressive interaction or a fast merging of the input-induced activity patterns.

4.4 Gated integrator model

The two-field model performs a continuous integration of input streams of any strength. This is a desirable feature for decision making since also weak evidence may bias decision processes involving multiple alternatives. One potential problem with the perfect integrator mechanism is that the pure accumulation of noise at field sites without specific input may in principle lead to the creation of bumps. Other neuro-inspired integrator models solve this problem by implementing a preset threshold mechanism that controls the minimum level of evidence entering the accumulation process (Cain et al. 2013; Koulakov et al. 2002). We propose a model extension inspired by experimental findings showing that neurons in local circuits may rapidly change their functional connectivity according to behavioral demands (Haider and McCormick 2009). In tasks requiring the accumulation of evidence, this modulation should affect the balanced excitation and inhibition in the local feedback loops responsible for the stabilization of population activity at any level. Only neurons that appear to be pre-activated by input above the noisy baseline should participate in these loops. The cellular and network mechanism by which functional connections are rapidly formed and broken are currently an active area of research (Haider and McCormick 2009). We apply the computationally simple idea of a state-dependent gating of the local coupling between the two fields by a threshold function $g(u)$. A step function with threshold $\kappa \leq \theta$ is used for simplicity. The model reads

$$\begin{aligned}\frac{\partial u(x,t)}{\partial t} &= -u(x,t) + v(x,t)g(u(x,t)-\kappa) \\ &\quad + I(x,t) + \epsilon^{1/2}\mathrm{d}W(x,t) \\ &\quad + \int_\Omega w(|x-y|)f(u(y,t)-\theta)\mathrm{d}y, \end{aligned} \tag{32a}$$

$$\begin{aligned}\frac{\partial v(x,t)}{\partial t} &= -v(x,t) + u(x,t)g(u(x,t)-\kappa) \\ &\quad - \int_\Omega w(|x-y|)f(u(y,t)-\theta)\mathrm{d}y. \end{aligned} \tag{32b}$$

The gating mechanism delays the perfect integration of evidence until a target location is selected by an initial input of strength $A_I > \kappa$, rendering a bump creation by accumulated (weak) noise unlikely. Figure 20 compares the pattern formation in response to an input at $x = 0$ in the stochastic model without (a) and with gating mechanism (c). Without gating, in addition to the input-driven bump at $x = 0$ various noise-induced bumps at other locations develop. The impact on noise integration can be seen when comparing the sum of $u(x)$ and $v(x)$, representing the total of accumulated external input and noise (b). For the gating case, the sum represents the bell-shaped input slightly corrupted by noise and small random fluctuations at other field sites (d). It is important to notice that the gating mechanisms does not destroy the exis-

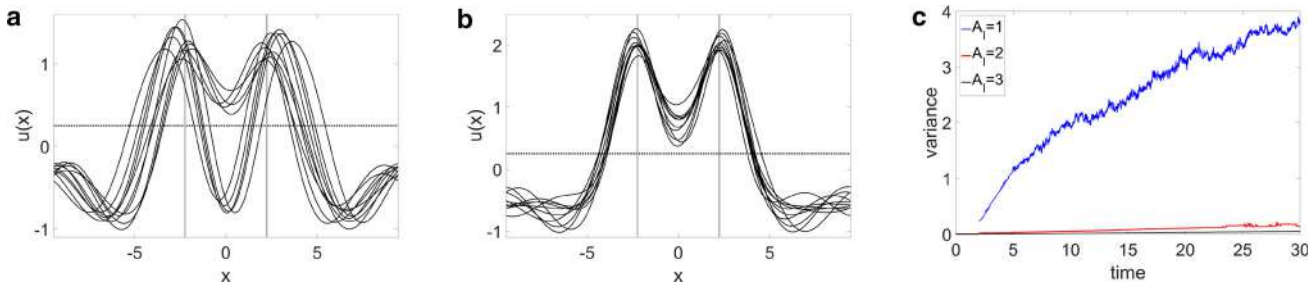

Fig. 18 Bump attraction/repulsion due to noise in the two-field model. Sample profiles of the u-population at time $t = 30$ created with two inputs with $A_{I_{1,2}} = 1$ (**a**) and $A_{I_{1,2}} = 3$ (**b**). The percentage of "merged" solutions for inputs with amplitudes $A_I \in \{1, 2, 3\}$ in $N = 500$ trials was respectively 60%, 98% and 100%. (**c**) Variance of the inter-peak distance as a function of time computed for $N = 500$ numerical simulations of the model for different input strengths A_I. The inputs with amplitudes $A_{I_{1,2}} = 1$, $A_{I_{1,2}} = 2$, $A_{I_{1,2}} = 3$, are applied at positions $x_{c_{1,2}} = \pm 2.25$. Remaining parameters of the inputs are $\sigma_{I_{1,2}} = 1$ and $d_I = 1$. The kernel w is given by (2) with $A_{ex} = 2$, $A_{in} = 1$, $\sigma_{ex} = 1.5$, $\sigma_{in} = 2.5$ and $w_{inh} = 0.1$. Threshold $\theta = 0.25$ (dotted line), $K = 0$, $\epsilon = 0.0025$, $L = 3\pi$, $\mathrm{d}x = 0.01$, $\mathrm{d}t = 0.01$

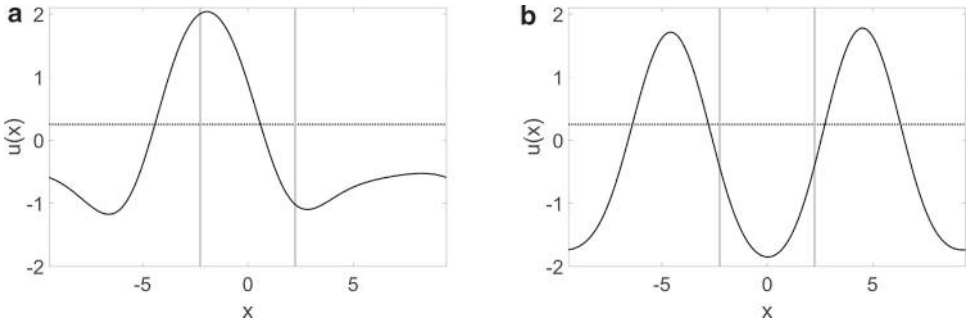

Fig. 19 Bump merging (**a**) and repelling (**b**) in the Amari model due to noise. The inputs with amplitudes $A_{I_{1,2}} = 1$ are applied at positions $x_{c_{1,2}} = \pm 2.25$. Remaining parameters of the inputs are $\sigma_{I_{1,2}} = 1$ and $d_I = 1$. Vertical lines indicate the sites $x_{c_{1,2}}$ where the inputs were applied. The kernel w is given by (2) with $A_{ex} = 2$, $A_{in} = 1$, $\sigma_{ex} = 1.5$, $\sigma_{in} = 2.5$ and $w_{inh} = 0.1$. Threshold $\theta = 0.25$ (dotted line), $\epsilon = 0.0025$, $L = 3\pi$, $\mathrm{d}x = 0.01$, $\mathrm{d}t = 0.01$

tence of subthreshold bumps since for sites x with $u(x) > \kappa$ a continuous integration of weak inputs is still supported.

The gating mechanism is also important for resetting stimulus-selective persistent activity to a homogeneous resting state. In WM applications of continuous attractor networks, it is typically assumed that a switch between a bump attractor and a stable resting state can be achieved by applying a transient inhibitory input to all neurons (Camperi and Wang 1998). Figure 21 illustrates this "forgetting" mechanism in a model simulation without noise. The neural integrator first develops a bump in response to a localized excitatory input which is followed by a strong decrease in activation when at time $t = 21$ the homogeneous inhibition is applied to the u-population. Functionally, the two fields become decoupled since $g(u) < \kappa$, $\forall x$, and the subthreshold activity in both layers converges to the homogeneous resting state, $u = v = 0$, as predicted by the Amari model (Amari 1977). Without the gating mechanism, the field dynamics would stabilize a subthreshold bump.

5 Discussion

Here we have presented a bump attractor model which is able to sustain localized activity patterns evoked by external inputs which differ in shape *and* amplitude. The model simulations demonstrate that the network dynamics not only supports the encoding of a single input value but also the storage of certain stimulus characteristics. This is in line with a growing body of experimental evidence showing a correlation between the level of persistent delay activity and stimulus attributes such as intensity/contrast (Constantinidis et al. 2001) or duration (Brody et al. 2003a). The possibility to stabilize localized activity patterns with a continuum of amplitudes can be in principle also used to model the experimentally observed dependence of persistent activity on task demands such as the amount of training (Qi et al. 2011; Histed et al. 2009) or varying choice certainty (Kiani and Shadlen 2009; Basso and Wurtz 1997). We have recently applied an extension of the two-field model to two spatial dimensions as part of a neuro-inspired robot control architecture for natural human-robot interactions. It implements the learning and

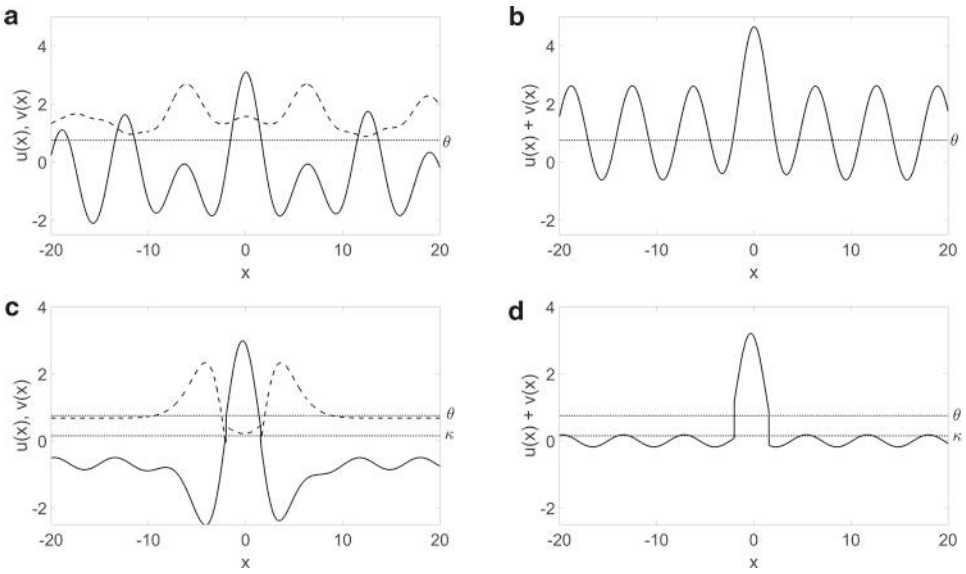

Fig. 20 Simulations of the two-field model (32) with different threshold values κ and the Mexican-hat connectivity given by (2) with $A_{ex} = 3$, $A_{in} = 1.5$, $\sigma_{ex} = 1.4$, $\sigma_{in} = 3$ and $w_{inh} = 0.2$, $\theta = 0.75$, $K = 1$. The spatial fluctuations are given by a cosine-correlated noise with $\epsilon = 0.005$. The bump at $x = 0$ is created with a localized input with $A_{I_1} = 2$, $\sigma_{I_1} = 1.5$, $d_I = 1$. (**a**,**b**) no gating; (**c**,**d**) $\kappa = 0.15$

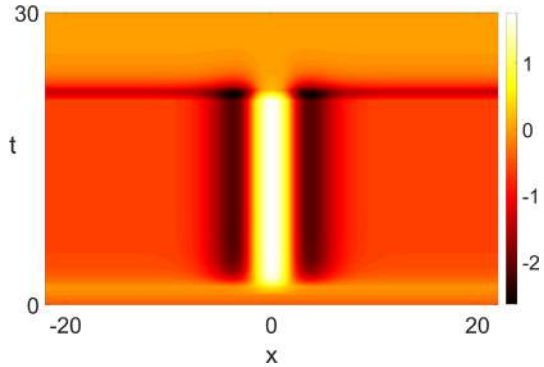

Fig. 21 Space-time plot showing the forgetting mechanism. A bump is first triggered by a localized input applied at $t = 1$. This is followed by a decay to resting state when at time $t = 21$ a homogeneous inhibitory input is applied to the u-population of (32). The connectivity function is given by (2) with $A_{ex} = 3$, $A_{in} = 1.5$, $\sigma_{ex} = 1.4$, $\sigma_{in} = 3$ and $w_{inh} = 0.2$. The localized input is defined by $A_{I_1} = 1$, $\sigma_{I_1} = 1.5$, $d_I = 1$ and the homogeneous inhibition by $A = -1.5$ and $d_I = 1$. Thresholds $\kappa = \theta = 0.5$, $K = 1$

adaptation of action planning and value-based decision making in a dynamic environment (Wojtak et al. 2021).

The model works as a robust neural integrator since the bump amplitude faithfully reflects the accumulation of input signals over time. This contrasts with the behavior of most attractor networks applied in working memory and decision making tasks in which the stable state corresponds to a stereotyped pattern of activity exclusively determined by the recurrent interactions within the network. The input dependence is achieved by combining a lateral-inhibition type network connectivity with local inhibitory and excitatory feedback mechanisms that are able to stabilize input-induced changes of the population activity at any level. A biophysically mechanistic formulation of the processing principles based on two coupled field equations of Amari-type is amenable to mathematical analysis. Being able to rigorously analyze the existence and stability of bump solutions and their dependence on model parameters is a major advantage over more complex, biophysically realistic models when trying to explain the behavior of cognitive agents.

Using an identical parameter set allowed us to directly compare the performance of the two-field model with the classical Amari model with Mexican-hat coupling. The network with the balanced local feedback exhibits several distinct features. First, two or more stable regions of excitation may exist at a distance where a gradient in the lateral inhibition profile predicts a merging or drifting of the bumps in the Amari model. Moreover, the lateral feedback excitation of the two-field model facilitates in general the formation of memory bumps. This is particularly evident in a sequential stimulus protocol in which lateral inhibition in the Amari model may prevent the encoding of an input in a stable activity pattern. This is true even for the case of a spatially uniform lateral inhibition for which a multi-bump solution exists. The two-field model thus predicts a higher working memory capacity without the need to refer to additional processing mechanism like top-down excitation (Edin et al. 2009) or a stimulus-selective synaptic facilitation (Mongillo et al. 2008). Second, the activation pattern induced by two nearby inputs do not merge completely into a single bump at an intermediate position but displays a wide plateau in its profile. This result is consistent with the prediction of biophysically realistic bump attractor networks (Wei et al. 2012) and has been described in electrophysiological stimulation studies (Vokoun et al. 2014). The higher uncertainty expressed by the wider activity distribution could be used by a downstream read-out system in cue integration and decision making tasks. Third, the two-field model supports the existence of stable subthreshold activity

patterns. In the context of the retro- cueing paradigm, we have argued that such patterns might represent less-salient items that become suppressed below threshold by means of lateral inhibition from bumps representing cued items. The experimental observation that neural memory representations often degrade to a large extent during the delay period has been taken as evidence for an active-silent state of working memory encoded in synaptic changes (Mongillo et al. 2008). The model simulations however suggest that postulating such a latent memory state might not be necessary at least for the retro- cueing task (Schneegans and Bays 2017). The information represented by weak sustained activity is not lost but can be restored with a spatially unspecific cue.

Unlike in bistable attractor models of Amari type, the baseline activity of the neural integrator is not a stable state. A forgetting mechanism can thus not be implemented by simply applying a sufficiently strong inhibitory input that destabilizes existing bumps. For working memory applications, we have proposed a simple gating mechanism for the local feedback which restores the stable resting state of the Amari model without destroying the existence of subthreshold bump solutions.

The possibility to represent stimulus attributes in the bump shape allows us to make predictions about the impact of for instance input strength (or contrast) on working memory performance. Simulations of the stochastic version of the two-field model reveal that the noise-induced drift of a single bump in the continuous attractor network decreases with increasing bump amplitude associated with stronger inputs. Larger bump amplitudes also greatly reduce the interaction effects of two input-induced bumps at a critical distance which can be described as repulsion or attraction when considering the relative peak positions. The neural integrator model shares the prediction that larger bumps provide more faithful input representations over time with the neural field model of lateral inhibition type introduced by Carroll et al. (2014). It consists of separate excitatory and inhibitory populations and implements a tight balance of excitation and inhibition within the network to support a continuum of possible bump amplitudes. Importantly, achieving this balance requires that the recurrent excitation is inversely proportional to the gain of a piecewise linear transfer function. Any change in the tuning of the form of the nonlinearity or the connectivity will destroy this balance. The two-field model is robust to such changes since the same connectivity and nonlinear transfer functions are used for the u-field and the v-field. An important consequence is that the assumption of a perfectly symmetric connectivity pattern in continuous bump attractor networks can be relaxed. Model simulations with a slightly asymmetric connectivity profile or a profile with random perturbations show that localized activity patterns with a biased or distorted shape are stabilized by the network dynamics. Mitigating the inherent structural instability of bump attractor models offers new perspective for applications of dynamic field theory that include for instance the learning of the connectivity pattern (Fotouhi et al. 2015). We will explore this line of research in future work.

The two-field model shares the robustness to global changes in the neural gain and perturbations of the translation-invariant network structure with the firing rate model of working memory proposed by Lim and Goldman (2013). It consists of pools of interconnected excitatory and inhibitory neurons that are able to maintain graded levels of spatially tuned patterns of persistent activity without widespread lateral inhibition. It implements principles of negative-derivative feedback control by assuming that positive feedback mediated by recurrent excitation and negative feedback mediated by recurrent inhibition have equal strength, but inhibition operates on a faster timescale. Perturbations that affect the tight excitation/inhibition balance disrupt the memory performance. Also the two-field model is sensitive to perturbations in the balance of recurrent inputs from neighboring neurons and the local inhibitory feedback that a neuron receives. For instance, applying a nonlinear response function with saturation for the v-population will cause a saturation limit of the input integration. However, it can be expected that lateral inhibition acts as a stabilizing factor if the imbalance is not too strong. Further work is needed to systematically investigate how changes applied to the gain, the amplitude or the spatial ranges of the recurrent interactions in just one of the fields affect the pattern formation process.

Acknowledgements The work received financial support from FCT through the PhD fellowship PD/BD/128183/2016 the project "Neurofield" (PTDC/MAT-APL/31393/2017) and the research centre CMAT within the project UID/MAT/00013/2020.

Availability of data and material Not applicable.

Declarations

Conflicts of interest The authors declare that they have no conflict of interest.

Code availability Example codes implemented in MATLAB are available at https://github.com/w-wojtak/A-dynamic-neural-field-model-of-continuous-input-integration.

A Numerical simulations

Numerical simulations of the model were done in MATLAB using a forward Euler method with parameters $L = 30$, $N = 12000$, $\mathrm{dx} = 2L/N = 0.005$, $T = 100$, $M = 10000$, $\mathrm{dt} = T/M = 0.01$, unless stated otherwise in specific examples. Numerical simulations of the stochastic model were done using the Euler-Maruyama method. To compute the

spatial convolution of w and f we employ a fast Fourier transform (FFT), using MATLAB's in-built functions `fft` and `ifft` to perform the Fourier transform and the inverse Fourier transform, respectively. Periodic boundary conditions are used. By choosing a sufficiently large domain size, we make sure that the localized patterns evolve sufficiently far from the boundaries.

For performing numerical continuation, we use the method described in (Rankin et al. 2014) and adapt MATLAB code available in (Avitabile 2016). The main advantage of this method is that it can be applied directly to the full integral model. This is possible due to the usage of Newton-GMRES solvers combined with a fast Fourier transform (FFT) employed for computing the convolution term (Rankin et al. 2014).

References

Almeida R, Barbosa J, Compte A (2015) Neural circuit basis of visuospatial working memory precision: a computational and behavioral study. J Neurophysiol 114(3):1806–1818

Amari S (1977) Dynamics of pattern formation in lateral-inhibition type neural fields. Biol Cybern 27(2):77–87

Amari SI (1980) Topographic organization of nerve fields. Bull Math Biol 42(3):339–364

Avitabile D (2016) Numerical computation of coherent structures in spatially-extended systems. Second International Conference on Mathematical Neuroscience, Antibes Juan-les-Pins, 2016

Basso MA, Wurtz RH (1997) Modulation of neuronal activity by target uncertainty. Nat 389(6646):66–69

Bays PM, Taylor R (2018) A neural model of retrospective attention in visual working memory. Cogn Psychol 100:43–52

Bicho E, Mallet P, Schöner G (2000) Target representation on an autonomous vehicle with low-level sensors. Int J Robot Res 19(5):424–447

Bogacz R (2007) Optimal decision-making theories: linking neurobiology with behaviour. Trends Cogn Sci 11(3):118–125

Brody CD, Hernández A, Zainos A, Romo R (2003a) Timing and neural encoding of somatosensory parametric working memory in macaque prefrontal cortex. Cerebral Cortex 13(11):1196–1207

Brody CD, Romo R, Kepecs A (2003b) Basic mechanisms for graded persistent activity: discrete attractors, continuous attractors, and dynamic representations. Current Opin Neurobiol 13(2):204–211

Cain N, Barreiro AK, Shadlen M, Shea-Brown E (2013) Neural integrators for decision making: a favorable tradeoff between robustness and sensitivity. J Neurophysiol 109(10):2542–2559

Camperi M, Wang XJ (1998) A model of visuospatial working memory in prefrontal cortex: recurrent network and cellular bistability. J Comput Neurosci 5(4):383–405

Carandini M, Heeger DJ (2012) Normalization as a canonical neural computation. Nat Rev Neurosci 13(1):51–62

Carroll S, Josić K, Kilpatrick ZP (2014) Encoding certainty in bump attractors. J Comput Neurosci 37(1):29–48

Compte A, Brunel N, Goldman-Rakic PS, Wang XJ (2000) Synaptic mechanisms and network dynamics underlying spatial working memory in a cortical network model. Cerebral Cortex 10(9):910–923

Constantinidis C, Wang XJ (2004) A neural circuit basis for spatial working memory. Neurosci 10(6):553–565

Constantinidis C, Franowicz MN, Goldman-Rakic PS (2001) The sensory nature of mnemonic representation in the primate prefrontal cortex. Nat Neurosci 4(3):311–316

Curtis CE, Lee D (2010) Beyond working memory: the role of persistent activity in decision making. Trends Cogn Sci 14(5):216–222

Denève S, Machens CK (2016) Efficient codes and balanced networks. Nat Neurosci 19(3):375–382

Edin F, Klingberg T, Johansson P, McNab F, Tegnér J, Compte A (2009) Mechanism for top-down control of working memory capacity. Proc Nat Acad Sci 106(16):6802–6807

Erlhagen W, Bicho E (2006) The dynamic neural field approach to cognitive robotics. J Neural Eng 3:36–54

Erlhagen W, Schöner G (2002) Dynamic field theory of movement preparation. Psychol Rev 109(3):545

Erlhagen W, Bastian A, Jancke D, Riehle A, Schöner G (1999) The distribution of neuronal population activation (DPA) as a tool to study interaction and integration in cortical representations. J Neurosci Methods 94(1):53–66

Ferreira F, Erlhagen W, Bicho E (2016) Multi-bump solutions in a neural field model with external inputs. Physica D: Nonlinear Phenomena 326:32–51

Ferreira F, Wojtak W, Sousa E, Louro L, Bicho E, Erlhagen W (2020) Rapid learning of complex sequences with time constraints: A dynamic neural field model

Fotouhi M, Heidari M, Sharifitabar M (2015) Continuous neural network with windowed Hebbian learning. Biol Cybern 109(3):321–332

French DA (2004) Identification of a free energy functional in an integro-differential equation model for neuronal network activity. Appl Math Lett 17(9):1047–1051

Gazzaley A, Nobre AC (2012) Top-down modulation: bridging selective attention and working memory. Trends Cogn Sci 16(2):129–135

Haider B, McCormick DA (2009) Rapid neocortical dynamics: cellular and network mechanisms. Neuron 62(2):171–189

Hebb DO (1949) The organization of behavior: a neuropsychological theory. Chapman & Hall, J Wiley, New York

Histed MH, Pasupathy A, Miller EK (2009) Learning substrates in the primate prefrontal cortex and striatum: sustained activity related to successful actions. Neuron 63(2):244–253

Jancke D, Erlhagen W, Dinse HR, Akhavan AC, Giese M, Steinhage A, Schöner G (1999) Parametric population representation of retinal location: Neuronal interaction dynamics in cat primary visual cortex. J Neurosci 19(20):9016–9028

Johnson JS, Spencer JP, Luck SJ, Schöner G (2009) A dynamic neural field model of visual working memory and change detection. Psychol Sci 20(5):568–577

Kiani R, Shadlen MN (2009) Representation of confidence associated with a decision by neurons in the parietal cortex. Sci 324(5928):759–764

Kilpatrick ZP, Ermentrout B (2013) Wandering bumps in stochastic neural fields. SIAM J Appl Dyn Syst 12(1):61–94

Koulakov AA, Raghavachari S, Kepecs A, Lisman JE (2002) Model for a robust neural integrator. Nat Neurosci 5(8):775–782

Krishnan N, Poll DB, Kilpatrick ZP (2018) Synaptic efficacy shapes resource limitations in working memory. J Comput Neurosci 44(3):273–295

Kubota S, Aihara K (2005) Analyzing global dynamics of a neural field model. Neural Process Lett 21(2):133–141

Kuo BC, Stokes MG, Nobre AC (2012) Attention modulates maintenance of representations in visual short-term memory. J Cogn Neurosci 24(1):51–60

Laing CR, Troy WC (2003) Two-bump solutions of Amari-type models of neuronal pattern formation. Physica D: Nonlinear Phenomena 178(3–4):190–218

Lim S, Goldman MS (2013) Balanced cortical microcircuitry for maintaining information in working memory. Nat Neurosci 16(9):1306–1314

Lin PH, Luck SJ (2009) The influence of similarity on visual working memory representations. Vis Cogn 17(3):356–372

Ma WJ, Jazayeri M (2014) Neural coding of uncertainty and probability. Annual Rev Neurosci 37:205–220

Masse NY, Rosen MC, Freedman DJ (2020) Reevaluating the role of persistent neural activity in short-term memory. Trends Cogn Sci 24(3):242–258

Miller EK, Cohen JD (2001) An integrative theory of prefrontal cortex function. Annual Rev Neurosci 24(1):167–202

Mongillo G, Barak O, Tsodyks M (2008) Synaptic theory of working memory. Sci 319(5869):1543–1546

Murray JD, Anticevic A, Gancsos M, Ichinose M, Corlett PR, Krystal JH, Wang XJ (2014) Linking microcircuit dysfunction to cognitive impairment: effects of disinhibition associated with schizophrenia in a cortical working memory model. Cereb Cortex 24(4):859–872

Owen MR, Laing CR, Coombes S (2007) Bumps and rings in a two-dimensional neural field: splitting and rotational instabilities. New J Phys 9(10):378

Qi XL, Meyer T, Stanford TR, Constantinidis C (2011) Changes in prefrontal neuronal activity after learning to perform a spatial working memory task. Cereb Cortex 21(12):2722–2732

Rankin J, Avitabile D, Baladron J, Faye G, Lloyd DJ (2014) Continuation of localized coherent structures in nonlocal neural field equations. SIAM J Sci Comput 36(1):B70–B93

Rhodes BJ, Bullock D, Verwey WB, Averbeck BB, Page MP (2004) Learning and production of movement sequences: Behavioral, neurophysiological, and modeling perspectives. Hum Mov Sci 23(5):699–746

Rolls ET, Dempere-Marco L, Deco G (2013) Holding multiple items in short term memory: a neural mechanism. PLOS ONE 8(4):e61078

Rose NS, LaRocque JJ, Riggall AC, Gosseries O, Starrett MJ, Meyering EE, Postle BR (2016) Reactivation of latent working memories with transcranial magnetic stimulation. Sci 354(6316):1136–1139

Sakai Y, Okamoto H, Fukai T (2006) Computational algorithms and neuronal network models underlying decision processes. Neural Netw 19(8):1091–1105

Schneegans S, Bays PM (2017) Restoration of fMRI decodability does not imply latent working memory states. J Cogn Neurosci 29(12):1977–1994

Schöner G (2016) Dynamic thinking: A primer on dynamic field theory. Oxford University Press, Oxford

Seung HS (1998) Continuous attractors and oculomotor control. Neural Netw 11(7–8):1253–1258

Soto D, Mäntylä T, Silvanto J (2011) Working memory without consciousness. Curr Biol 21(22):R912–R913

Souza AS, Oberauer K (2016) In search of the focus of attention in working memory: 13 years of the retro-cue effect. Atten Percept Psychophys 78(7):1839–1860

Sprague TC, Ester EF, Serences JT (2016) Restoring latent visual working memory representations in human cortex. Neuron 91(3):694–707

Sutterer DW, Foster JJ, Adam KC, Vogel EK, Awh E (2019) Item-specific delay activity demonstrates concurrent storage of multiple active neural representations in working memory. PLOS Biol 17(4):e3000239

Trübutschek D, Marti S, Ojeda A, King JR, Mi Y, Tsodyks M, Dehaene S (2017) A theory of working memory without consciousness or sustained activity. Elife 6:e23871

Vokoun CR, Huang X, Jackson MB, Basso MA (2014) Response normalization in the superficial layers of the superior colliculus as a possible mechanism for saccadic averaging. J Neurosci 34(23):7976–7987

Wang XJ (2003) Persistent neural activity: experiments and theory. Cereb Cortex 13(11):1123–1123

Wang Z, Kruijne W, Theeuwes J (2012) Lateral interactions in the superior colliculus produce saccade deviation in a neural field model. Vis Res 62:66–74

Wei Z, Wang XJ, Wang DH (2012) From distributed resources to limited slots in multiple-item working memory: a spiking network model with normalization. J Neurosci 32(33):11228–11240

Wildegger T, Humphreys G, Nobre AC (2016) Retrospective attention interacts with stimulus strength to shape working memory performance. PLOS ONE 11(10):e0164174

Wilimzig C, Schneider S, Schöner G (2006) The time course of saccadic decision making: Dynamic field theory. Neural Netw 19(8):1059–1074

Wimmer K, Nykamp DQ, Constantinidis C, Compte A (2014) Bump attractor dynamics in prefrontal cortex explains behavioral precision in spatial working memory. Nat Neurosci 17(3):431–439

Wojtak W, Coombes S, Bicho E, Erlhagen W (2016) Combining spatial and parametric working memory in a dynamic neural field model. In: Artificial Neural Networks and Machine Learning — ICANN 2016, Lecture Notes in Computer Science, Springer, vol 9886, pp 411–418

Wojtak W, Ferreira F, Bicho E, Erlhagen W (2019) Neural field model for measuring and reproducing time intervals. In: Tetko IV, Kůrková V, Karpov P, Theis F (eds) Artificial Neural Networks and Machine Learning - ICANN 2019: Theoretical Neural Computation. Springer International Publishing, Cham, pp 327–338

Wojtak W, Ferreira F, Vicente P, Louro L, Bicho E, Erlhagen W (2021) A neural integrator model for planning and value-based decision making of a robotics assistant. Neural Comput Appl 33:3737–3756

Wu S, Hamaguchi K, Amari Si (2008) Dynamics and computation of continuous attractors. Neural Comput 20(4):994–1025

Zylberberg J, Strowbridge BW (2017) Mechanisms of persistent activity in cortical circuits: possible neural substrates for working memory. Annual Rev Neurosci 40:603–627